

---

Technologia i Automatykacja Montaży  
Assembly Techniques and Technologies

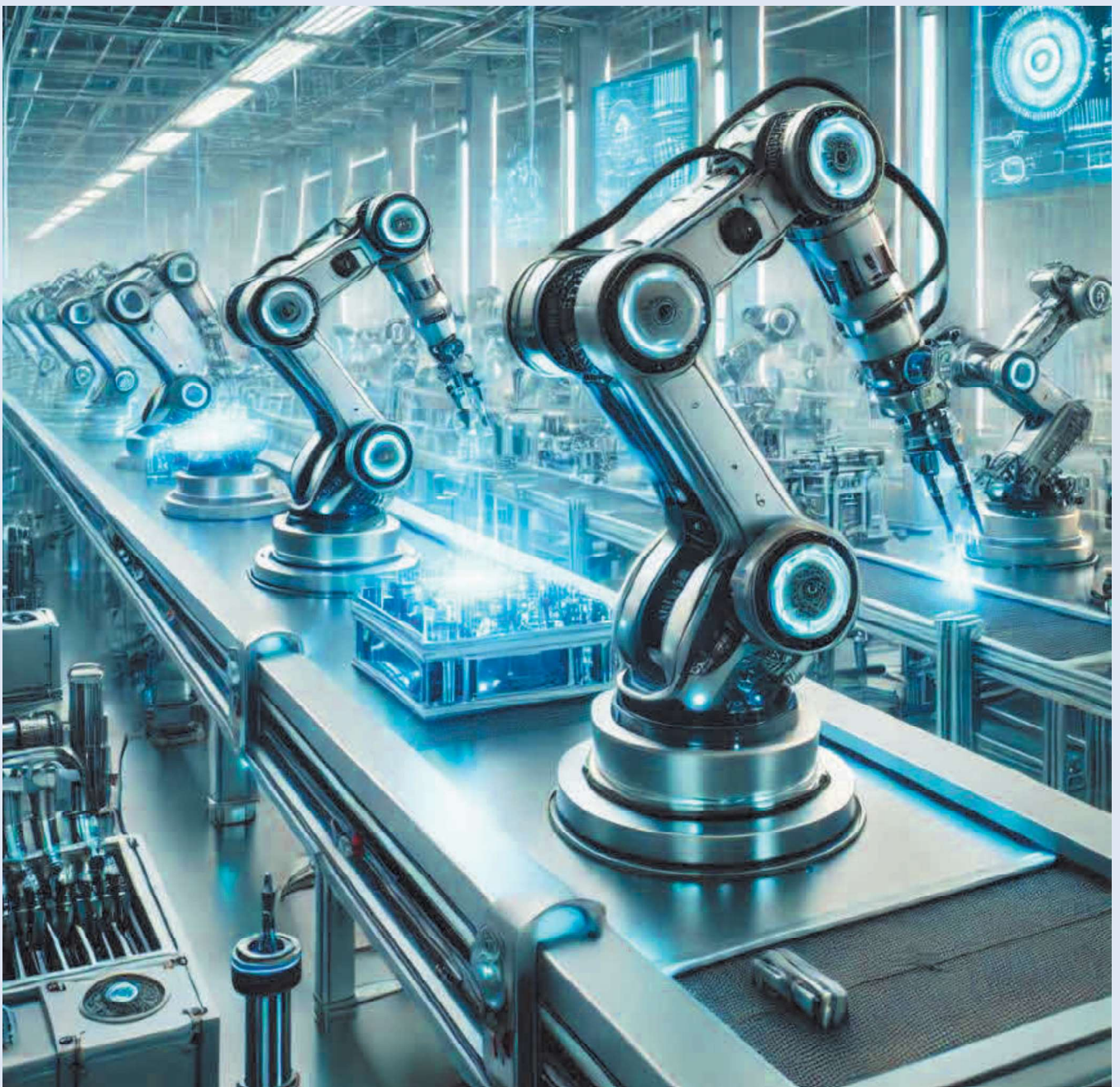
**TIAM**

Technologia i Automatykacja Montaży

Open Access: [journals.prz.edu.pl/tiam](https://journals.prz.edu.pl/tiam) • e-ISSN-2450-8217 • Volume 125, Issue 3, 2024

---

Publisher: Łukasiewicz Research Network – Warsaw Institute of Technology • Rzeszow University of Technology • Patronage SIMP • Since 1993



**RZESZOW UNIVERSITY  
OF TECHNOLOGY**



**Łukasiewicz**  
Warsaw Institute of Technology

## CONTENTS

---

**3**

Jan Godzimirski, Andrzej Komorek

**A proposal for a new method of testing the impact strength of adhesive joints**

*Propozycja nowej metody badania udarności połączeń klejowych*

**12**

Tomasz Samborski, Andrzej Zbrowski, Stanisław Kozioł

**Horizontal laminar flow cabinet with a low background and clean air**

*Pozioma komora laminarna z niskim tłem i czystym powietrzem*

**21**

Elżbieta Doluk, Izabela Miturska-Barańska, Oleksandra Krupowych

**Accuracy of assembly holes after drilling in Al/CFRP layered structure**

*Dokładność wykonania otworów montażowych po wierceniu konstrukcji warstwowej typu Al/CFRP*

**29**

Abigail Machaj, Kinga Sobczyk, Wiktoria Wojnarowska, Michał Wanic

**Design for assembly: wrist orthosis design concepts proposals**

*Projektowanie pod kątem montażu: propozycje koncepcji ortez nadgarstka*

**38**

Arkadiusz Garwol

**Jet engine – construction and modern development examples**

*Turbinowy silnik odrzutowy – budowa i przykłady obecnego rozwoju*

**44**

Robert Tomasiewicz

**Modular technological line for assembling and testing car dampers**

*Modułowa linia technologiczna do montażu i testowania amortyzatorów samochodowych*



Quarterly „Technologia i Automatykacja Montaży” is listed on the list of scored journals of Polish Ministry of Education and Science - 40 points.

## A PROPOSAL FOR A NEW METHOD OF TESTING THE IMPACT STRENGTH OF ADHESIVE JOINTS

### PROPOZYCJA NOWEJ METODY BADANIA UDARNOŚCI POŁĄCZEŃ KLEJOWYCH

Jan GODZIMIRSKI<sup>1</sup> , Andrzej KOMOREK<sup>2</sup> 

<sup>1</sup> Faculty of Mechatronics, Armament and Aerospace, Military University of Technology, Warsaw, Poland

<sup>2</sup> Department of Aviation, Polish Air Force University Dęblin, Poland

\* Corresponding author: [jan.godzimirski@wat.edu.pl](mailto:jan.godzimirski@wat.edu.pl)

#### Abstract

The usefulness of the proprietary method of testing the impact strength of adhesive joints under shear loads was checked. An adhesively bonded lap sample of flat bars with a thickness of 5 mm, loaded on the side surface of the overlap, was proposed. Numerical calculations have shown that in such a loaded lap joint, shear stresses dominate. Impact tests of such specimens can be performed on conventional Charpy hammers. Experimental tests were carried out on samples made of steel, brass and aluminum alloy bonded with various adhesives: Epidian57/Z1, Raychem S1125, Loctite 9464 and DP 420. The conducted experimental tests showed high reproducibility of the results of such tests and as expected, higher destruction energy of flexible adhesive and adhesive layers of greater thickness was obtained.

**Keywords:** adhesive joints, impact strength of adhesive joints, new impact testing method

#### Streszczenie

Sprawdzono przydatność autorskiej metody badania udarności połączeń klejonych obciążonych na ścinanie. Zaproponowano klejoną na zakładkę próbkę wykonaną z płaskowników o grubości 5 mm, obciążaną na bocznej powierzchni zakładki. Obliczenia numeryczne wykazały, że w tak obciążonym złączu zakładkowym dominują naprężenia styczne. Próby udarności takich próbek można wykonywać na konwencjonalnych młotkach Charpy'ego. Przeprowadzono badania eksperymentalne na próbkach wykonanych ze stali, mosiądzu i stopu aluminium klejonych różnymi klejami Epidian57/Z1, Raychem S1125, Loctite 9464 oraz DP 420. Przeprowadzone badania eksperymentalne wykazały dużą powtarzalność wyników takich badań i zgodnie z oczekiwaniami uzyskano wyższą energię niszczenia kleju elastycznego i warstw kleju o większej grubości.

**Słowa kluczowe:** klucze: połączenia klejowe, udarność połączeń klejowych, nowa metoda badań udarności

## 1. Introduction

Adhesive bonded is one of the methods of joining parts. The factor driving the dynamic development of the adhesive technique is, above all aviation and cosmonautics as well as the automotive industry (Adams 1997, Higgins 2009, Silva 2011) and construction. In addition to testing static properties, for some time now more and more tests have been carried out on the resistance of adhesive joints to impact loads. This especially applies to vehicles exposed to various

types of collisions (Grant 2009, Galvez 2017, Machado 2018).

Currently, three methods of testing the impact strength of adhesive joints are recommended:

- Block Shear Test (ISO 9653) (Adams 2016, Taylor 1996, Asgharifar 2014),
- Impact Wedge Peel Test (ISO11343, Blacman 2000, Gyeong-Seo 2020),



- Impact shear method of lap joints subjected to tensile loading (Adamvalli 2014, Raykhere 2010, Komorek 2021).

The first two methods are standardized. The first is like the standard for wood adhesives. It consists in adhesively bonding a plate 3 mm thick, 25 mm wide and 10 mm long (Fig. 1) to a metal block, which is dynamically loaded with a hammer impactor (Fig. 2) during the tests. The result of the experiment depends on the direction of the impact. The destruction energy of the adhesive joint is measured, and divided by the joint surface, it is possible to calculate the impact strength of the tested joint.

The main disadvantage of this method is the low reproducibility of the experiment results, the reasons explained in publications (Adams 1966, Komorek 2016) are difficult to eliminate.

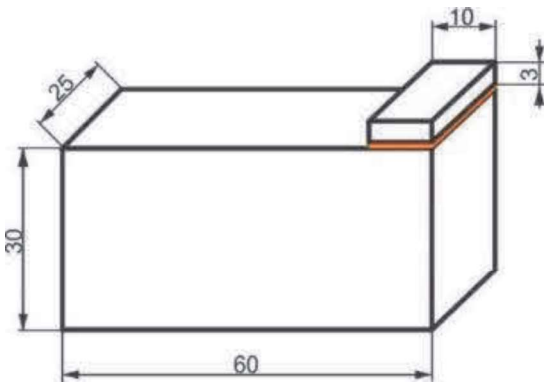


Fig. 1. Block sample

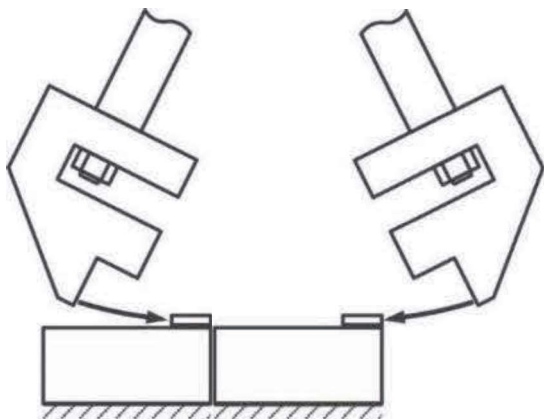


Fig. 2. Block sample load

An attempt to modify this method by changing the shape of the adhesively bonded element to cylindrical (Fig. 3) allowed to reduce the scatter of the test results but led to plastic deformation of the loaded element (Fig. 4), which resulted in the accumulation of stresses in the adhesive layer near the striking edge (Komorek, 2020).

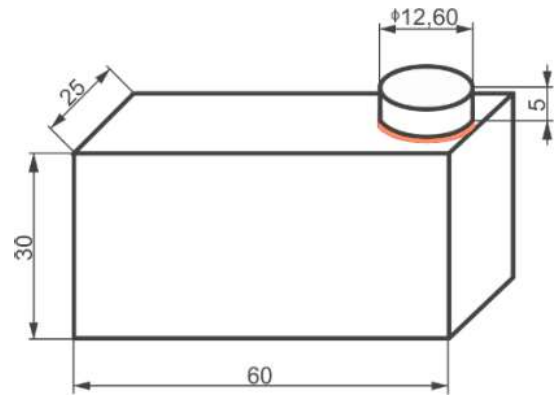


Fig. 3. Modified block sample

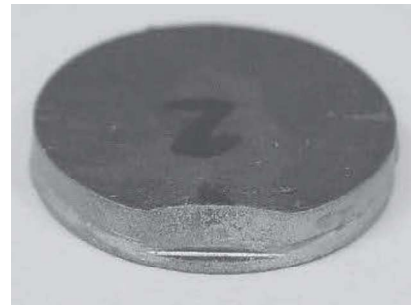


Fig. 4. Plastic deformation of the cylindrical plate under dynamically loaded

Due to the disadvantages of the block connection test method, such tests are rarely conducted.

The ISO11343 method, consisting in dynamic cleaving of the adhesive joint with a wedge (Fig. 5), is more widely used.

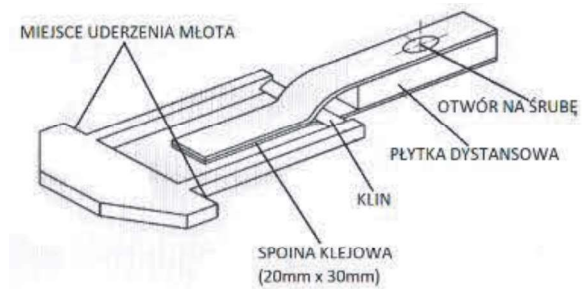


Fig. 5. The method of dynamic cleaving the adhesive joint with a wedge

This method is used in the automotive industry to test the crash test resistance of adhesively bonded car bodies. It requires a specialized device measuring and recording the dependence of force on time or force on displacement, which, after integration, allows the energy to be determined between 25% and 90% of the curve. The results of such tests depend on the properties of the adhesive, the surface treatment of the joined elements (adhesion forces) and the mechanical properties of the bonded materials. Such tests are essentially dynamic peel tests.

Due to the fact, that a properly designed adhesive joint should be mainly stressed for shear, attempts are made to test the impact strength of lap joints. Due to the lack of an appropriate standard, researchers use their own solutions, which makes it difficult to compare the obtained results.

The authors conducted tests on lap specimens made of two plates with dimensions of 20x100 mm and a thickness of 2 mm. A pendulum hammer with a modified striker shape was designed to conduct such research (Fig. 6).

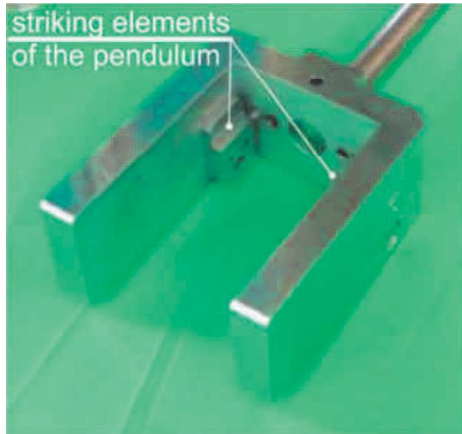


Fig. 6. Modified striker of a hammer

At one end of the adhesively bonded lap sample, a special holder with a wedge was attached (Fig. 7), which prevented the sample from moving in the holder during loading.

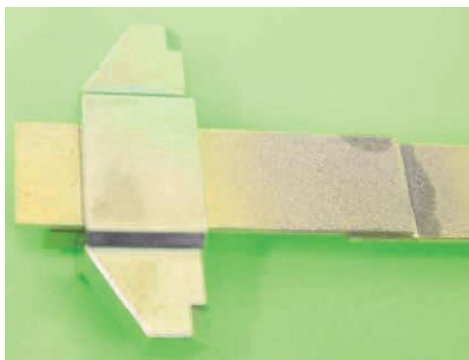


Fig. 7. A lap specimen with a handle

The other end of the sample was fixed in a rigid holder (Fig. 8) and a hammer hit a self-clamping holder fixed on the sample.

The impact tests carried out in accordance with the presented method were characterized by a much

greater reproducibility of the results than in the tests of block joints, although it was not possible to eliminate the removal of samples from the holders (about 10%), which resulted in a rapid increase in the measured energy.



Fig. 8. The sample attached to the impact tests

The presented test method allows to study the effect of the overlap length, the thickness of the adhesive layer, the method of preparing the surface for bonding and the stiffness of the sheets to be bonded on the impact strength of the joints. Its disadvantage is the labor-consumption of such tests resulting from careful assembly of samples and the need to have a pendulum hammer with a modified structure. Considering the limitations of the test method for lap specimens, another method of testing the impact shear resistance of adhesive joints has been proposed. The theory of strength of adhesive joints shows that there are three basic structural systems of such joints, in the adhesive layers of which shear stresses dominate (Silva, 2011) (Fig. 9).

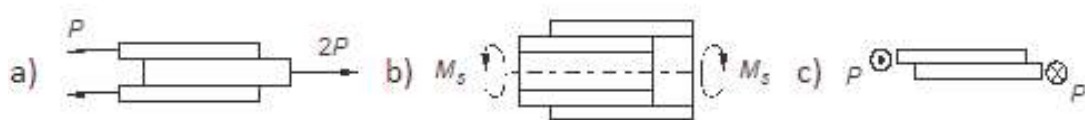


Fig. 9. Models of shear-loaded adhesive joints (a - lap, b - sleeve-twisted, c - lap-stressed along the width of the overlap)

The aim of the analysis was to check the suitability for impact tests of samples loaded similarly to the third load model presented in Fig. 9.

## 2. Numerical analysis

It was assumed that the sample will have similar dimensions to the samples used in the impact tests of metals and it will be possible to perform the tests on commonly available Charpy pendulum hammers. The sample load model and its numerical model of such a sample is shown in Fig. 10.

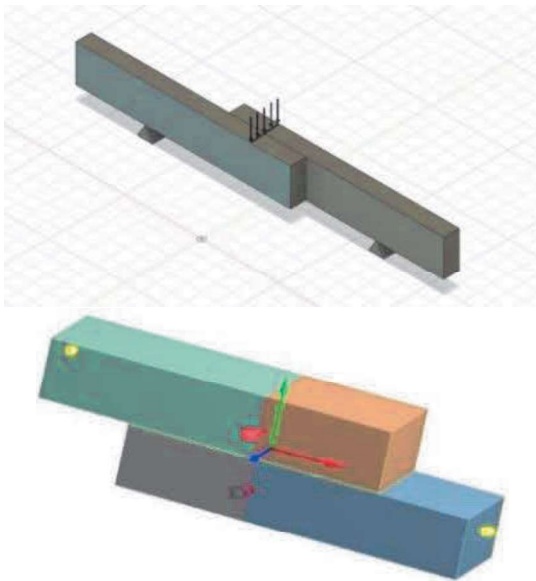


Fig. 10. Model of sample mounting and loading

The adhesively bonded elements were given the properties of an aluminum alloy ( $E = 72$  GPa,  $\nu = 0.33$ ), and an adhesive layer with a thickness of 0.15 mm was given the properties of epoxy adhesive ( $E = 2$  GPa,  $\nu = 0.35$ ). The sample was supported on both sides (spacing of supports 43 mm) and centrally loaded with a total force of 2000 N distributed evenly along the edge. The calculation results are shown in Figs. 11 to 14.

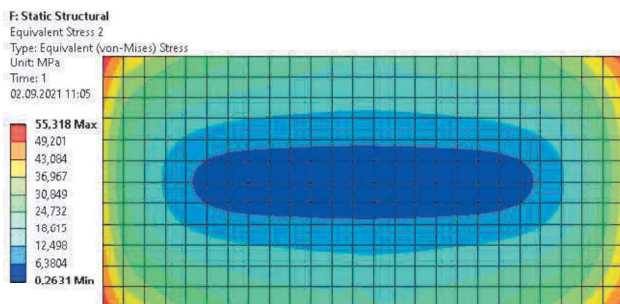


Fig. 11. The von Mises stress distribution in the adhesive layer

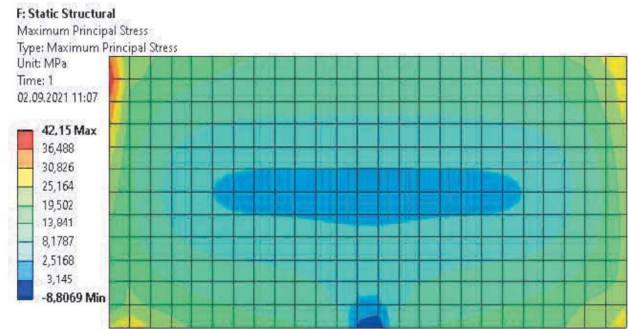


Fig. 12. Distribution of the maximum principal stresses in the adhesive layer

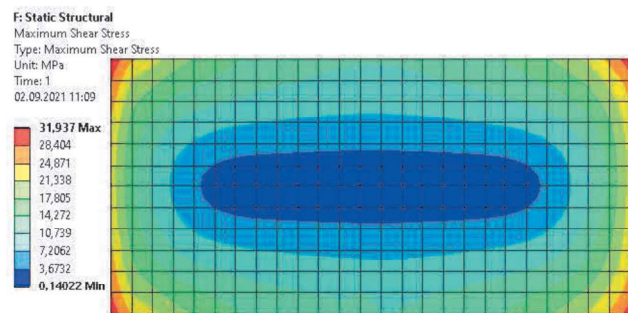


Fig. 13. Distribution of maximum shear stresses in the adhesive layer

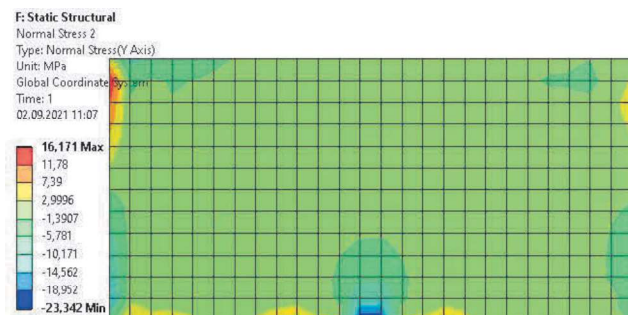


Fig. 14. Distribution of normal stresses perpendicular to the adhesive layer surface

The performed calculations show that shear stresses dominate in the adhesive layer of the analyzed joint, to a greater extent than in lap joints. It follows that the proposed samples meet the criterion of joints loaded in shear and can be used in impact tests.

Additionally, numerical calculations were carried out in which the type of bonded materials (Young's modulus) was changed, the length of the overlap and the thickness of the bonded elements under the same load. The results of these calculations are presented in Table 1.

**Table 1.** The relationship of stresses in the adhesive layer on the type of joined materials, the thickness of the bonded elements and the length of the overlap

Overlap	Thickness of the joined elements 6 mm				Thickness of the joined elements 5 mm		
	15 mm	25 mm			25 mm		
Material	duralumin	duralumin	brass	steel	duralumin	brass	steel
Stresses [MPa]							
$\sigma_{VM}$	68.4	55.3	48.9	41.9	59.7	52.4	44.4
$\sigma_I$	55.5	42.2	35.0	28.2	45.2	37.3	29.8
$\tau_{max}$	39.5	31.9	28.3	24.2	34.5	30.2	25.6
$\sigma_Y$	22.8	16.2	11.6	7.5	17.3	12.5	8.1

$\sigma_{VM}$  – von Mises stress,  $\sigma_I$  – maximum principal stress,  $\tau_{max}$  – maximum shear stress,  $\sigma_Y$  – normal stress perpendicular to the adhesive layer surface

The calculations show that in the case of standardization of such a test method, the length of the overlap, the thickness of the bonded elements and their width should be determined. When changing the distance between the supports from 43 to 60 mm, the calculated stresses increased by about 50%. If we assume that the criterion of dynamic failure was only the value of stresses in the adhesive layer, then the highest failure energy should be obtained for steel samples of greater thickness, jointed with a longer lap and with a smaller spacing of support.

### 3. Research methodology

Rectangular cross-section bars with dimensions of 12x5 or 12x6 mm were cut into 45 mm long sections. On one side of the sample, a surface with a side length of 25 mm intended for adhesive bonding was marked. The joined surfaces were prepared for adhesive bonding using various methods: only degreasing with extraction gasoline, roughening with abrasive cloth No. 80 and degreasing with gasoline, or sandblasting with corundum and degreasing with gasoline. Two elements made of a 12x5 mm flat bar 45 mm long each were adhesively bonded, with an overlap of 25 mm. The bonded elements were made of brass M69, steel C45 and aluminum alloy AW 3035 H12).

Adhesives were applied to both dried surfaces. To obtain the appropriate thickness of the adhesive layers, sewing threads were placed in them or not. Epidian 57 resin was mixed with the Z1 hardener in weight proportions of 100 to 10.5. The ingredients of other adhesives are dosed automatically while squeezing them from the packaging. The samples were bonded in a special device with low contact pressures exerted by springs. The adhesives were cured according to the manufacturers' recommendations (Epidian 57 - 24 h at ambient temperature and 5 h at 80°C, Loctite 9464 – 7 days at ambient temperature, DP 420 – 48 h at ambient temperature, Raychem – 24 hours at ambient temperature).

After the joints had hardened, the adhesive flashes were removed using a metal cutting saw blade and an abrasive cloth. The samples were mounted centrally in swing hammers. The experiment was conducted mainly on a SW – 5 swing hammer with an energy of 50 J and a speed of 3.8 m/s with a support spacing of 43 mm (Fig. 15) and on a pendulum hammer Julietta with the energy of 7.5 J with a spacing of supports 60 mm (only one batch of samples).



**Fig. 15.** Sample placed on a pendulum hammer

Five samples in each batch were tested and the energy of destruction of joints was recorded (Fig. 16). The results were analyzed statistically by calculating the mean value and confidence intervals at the 95% significance level.



**Fig. 16.** A batch of brass samples bonded with Epidian 57 / Z1 adhesive

#### 4. Experimental tests

In the first stage of the research, the influence of the thickness of the adhesive layers and their stiffness on the impact strength of the joints was estimated. The adhesively bonded surfaces were roughened with abrasive cloth of granulation 80 and washed with gasoline. Three batches brass samples of 5 pieces each, were bonded with adhesive: Epidian57 / Z1 (thickness of adhesive layer 0.04 mm), Epidian 57 / Z1 (thickness of adhesive layer 0.3 mm) and Raychem S-1125 characterized by great flexibility (thickness of adhesive layer 0.25 mm) and one batch of steel and aluminum alloy samples were bonded with Epidian 57 / Z1 adhesive (thickness of the adhesive layer 0.3 mm).

The tests were carried out on a pendulum hammer SW – 5. The nature of the destruction of the adhesive layers of brass samples is shown in Fig. 17.

The results of the tests with confidence intervals for the 95% level of significance are presented in Table 2.

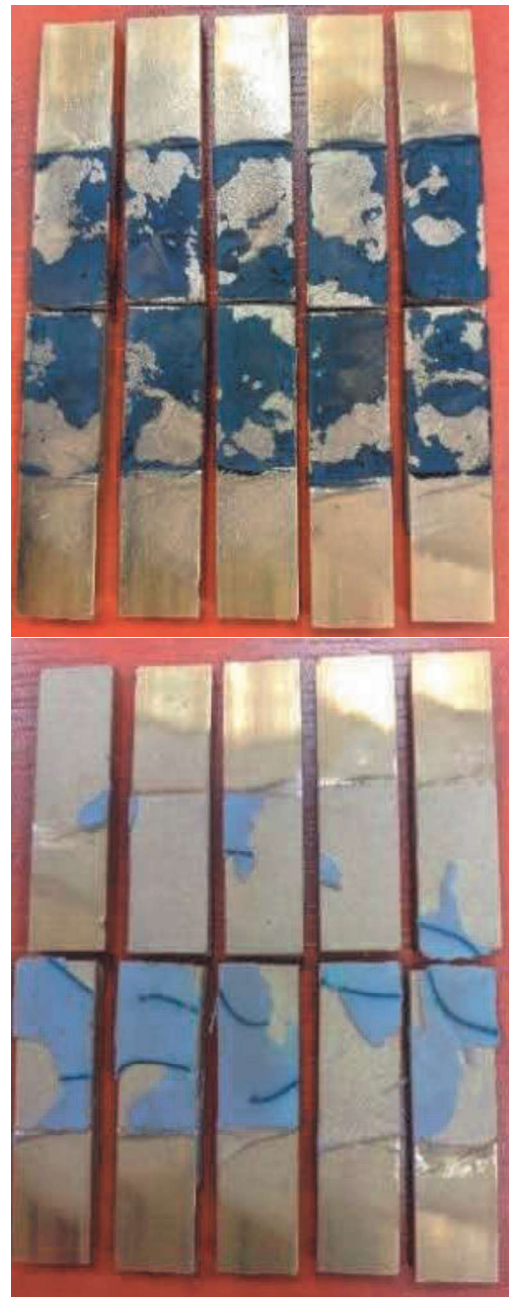


**Fig. 17.** The nature of destruction of adhesive layers with a thickness of 0.3 mm (Epidian 57 / Z1 adhesive) and 0.25 mm (Raychem adhesive)

**Table 2.** Results of impact tests

Adhesive	Epidian57/Z1 g = 0.04 mm	Epidian57/Z1 g = 0.3 mm	Raychem g = 0.25 mm	Epidian57/Z1 g = 0.3 mm	Epidian57/Z1 g = 0.3 mm
Material	brass			steel	AW 3035
Energy [J]	1.8	2	3.5	1.5	2.3
	1.7	2	3	1.3	2.4
	1.6	1.8	3.6	1.4	2.1
	1.7	2.1	2.8	1.5	1.7
	1.7	2.2	3.1	1.6	2.3
Average energy [J]	1.7±0.03	2.02±0.18	3.2±0.46	1.44±0,19	2.08±0,33

The test results are characterized by satisfactory repeatability and as expected, a significant influence of the adhesive layer thickness and adhesive stiffness on the impact strength of the tested joints.

The impact strength of steel and brass specimens adhesively bonded with Loctite EA 9464 adhesive was also compared with different spacing of supports. In this case, the tests were carried out on a pendulum hammer Julietta with a spacing of supports 60 mm. The results of the specified energies are shown in Table 3.

**Table 3.** Comparison of the failure energy of brass and steel samples bonded with Loctite EA 9464 adhesive, tested at different spacing of supports (steel samples only washed with gasoline, brass samples roughened with cloth 80 and degreased)

Spacing of supports	60	43
Material	Average energy of failure [J]	
steel	1.48±0.22	1.88±0.26
brass	2.43±0.36	4.12±0.22

According to the results of numerical calculations, the increase in the spacing of supports resulted in a decrease in the energy of joint destruction.

Even though in the adhesive layers of steel samples there are lower stresses than in the brass samples under the same static load, their impact strength turned out to be lower. This may be due to the different adhesion of the adhesive to different materials or the lower impact strength of the stiffer joints.

To compare the adhesive properties of steel, brass and aluminum alloy surfaces prepared for bonding by various methods the tension strength tests were carried out on cylindrical samples (Fig. 18) bonded with Loctite EA 9464 adhesive.

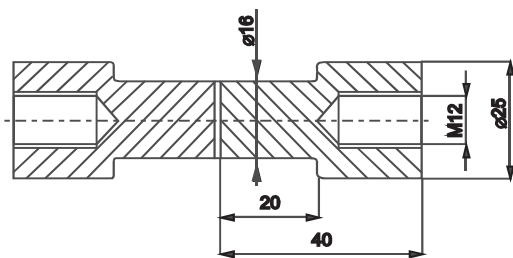


**Fig. 18.** A sample for testing the tension strength of adhesives

**Table 4.** Tensile strength test results for Loctite EA 9464 adhesive bonding various materials

Surface treatment	Roughening with cloth 80 and degreasing			Degreasing
	AW 3035	Brass	Steel	Steel
Strength, MPa	26.4 ±2.35	37.1 ±2.1	31.5 ±2.3	17.59 ±0.35

The research shows that when the surface preparation for adhesively bonding with Loctite EA 9464 is roughened with cloth no. 80, better adhesive properties are shown by brass than steel and aluminum alloy. Only the degreasing of steel surfaces with gasoline resulted in a significant decrease in the tensile strength of steel samples (about 50%).

Table 5 compares the impact toughness of samples made of different metals bonded with Loctite EA 9464.

**Table 5.** Comparison of the failure energy of samples made of various materials bonded with Loctite EA 9464 adhesive (surface treatment with abrasive cloth No. 80)

Material	AW 3035	Brass	Steel
Failure energy, J	4.43±0.80	4.12±0.42	5.68±0.27

The impact energy destruction of samples was also tested, the surfaces of which were prepared for bonded by sandblasting with electrocorundum and then washing with gasoline. The test results are presented in Table 6 (tests were performed twice).

**Table 6.** Comparison of the failure energy of samples made of various materials adhesively bonded with Loctite EA 9464 (sandblasting of bonded surfaces)

Material	AW 3035	Brass	Steel
Failure energy, J	3.00±0.44	6.04±0.48	4.45±0.28
	2.92±0.26	5.06±0.57	4.57±0.12

The use of such a method of surface preparation resulted in a significant increase in the destruction energy of steel lap specimens loaded on the side surface as well as brass specimens, but a decrease in the energy of aluminum alloy specimens. This proves the relevant influence of the adhesive forces on the impact strength of adhesive joints.

Considering the high heat capacity of the samples and the speed of performing the impact tests, tests of the influence of temperature on the impact strength of adhesive joints were carried out. The tests were carried out on steel samples, sandblasted, adhesively bonded with two adhesives: Loctite 9464 and DP 420. The destruction energy of joints at ambient temperature and heated in a laboratory oven to 60°C was tested. To eliminate the effect of increased temperature on the hardening of the adhesive, all samples were annealed at 60°C, and some of the samples intended for testing at ambient temperature were then cooled. The test results are presented in table 7.

**Table 7.** Comparison of the destruction energy of steel samples at ambient and elevated temperature of 60°C

Adhesive	Loctite 9464		DP 420	
Temperature	20°C	60°C	20°C	60°C

For both adhesives, a significant decrease in the impact strength of the tested joints was found at an elevated temperature of 60°C. An inverse relationship was expected, as the adhesive layer will become more flexible with increasing temperature. It was assumed that the reason for the decrease in impact strength may be stresses caused by different values of linear expansion coefficients of steel and adhesives.

Numerical calculations were carried out in the ANSYS 19 system, in which the sample was first loaded with a force of 6600 N (resulting from tests of the static strength of such joints), and then with the same force and a temperature increase of 40°C.

For steel, the value of the linear expansion coefficient  $\alpha = 1.2 \cdot 10^{-5} \text{ 1/C}$  was declared, and for the adhesive  $\alpha = 5 \cdot 10^{-5} \text{ C. temperature change}$ .

Fig. 19 and 20 show the distributions of the maximum principal stresses in the adhesive layers: loaded with force and loaded with force and temperature change.

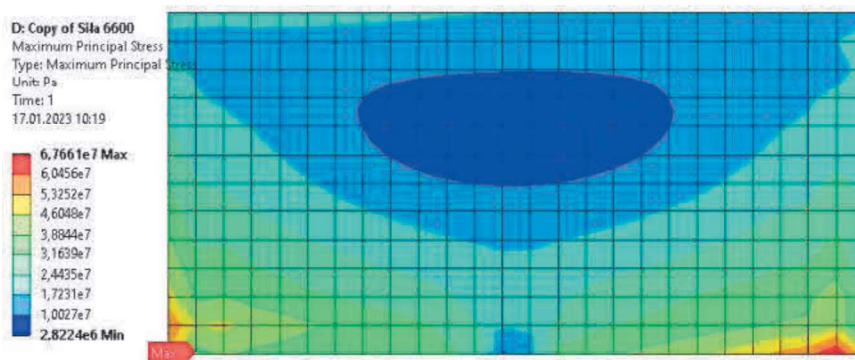


**Fig. 19.** Maximum principal stresses in the adhesive layer loaded with a force of 6600 N

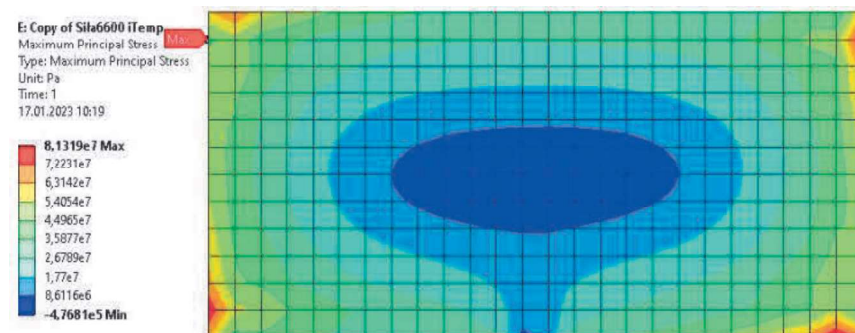


**Fig. 20.** Maximum principal stresses in the adhesive layer loaded with a force of 6600 N and a temperature increase of 40°C

Even though the load on the joint with only a temperature increase of 40°C generated stresses in the adhesive layer of about 2.5 MPa, the increase in stresses in the adhesive layer loaded with force due to the temperature increase was 13.6 MPa, i.e. it had a significant impact on the joint effort.

### 5. Conclusion

In the joints of the samples tested according to the proposed method, shear stresses dominate, i.e. those that occur in properly designed adhesive joints.

The impact test in accordance with the proposed method is characterized by a much greater repeatability of results than in the case of testing block

or lap samples, which allows to reduce the number of tested samples.

The tests can be carried out on typical pendulum hammers with energies of 10 J, and the adhesively bonded elements can be reused several times in the tests after removing the adhesive from the previous tests.

Considering the relatively high thermal capacity of the proposed samples and the speed of the tests, the proposed method enables the study of the influence of temperature on the impact strength of adhesive joints.

## References

- Adams R.D., Harris J.A. 1996 "A critical assessment of the block impact test for measuring the impact strength of adhesive bonds" *International Journal of Adhesion and Adhesives* 16: 61-71.
- Adams R.D., Comyn J. Wake W.C. 1997. Structural adhesive joint in engineering, Springer Science & Business Media, London.
- Adamvalli M., Parameswaran V. 2008 "Dynamic strength of adhesive single lap joints at high temperature" *International Journal of Adhesion and Adhesives* 28: 321-327.
- Asgharifar M, Kong F, Carlson, B, Kovacevic R. 2014 "Dynamic analysis of adhesively bonded joint under solid projectile impact" *International Journal of Adhesion and Adhesives* 50: 17-31.
- Blackman B.R.H, Kinloch A.J, Taylor A.C, Wang Y. 2000 "The impact wedge-peel performance of structural adhesives" *J. Materials Science* 35: 1867-1884.
- Galvez P. Quesada A., Martinez M.A., Abenojar J., Boada M.J.L., Diaz V. 2017 "Study of the behaviour of adhesive joints of steel with CFRP for its application in bus structures" *Composites Part B: Engineering* 129: 41-46.
- Grant L.D.R., Adams R.D., da Silva L.F.M. 2009 "Experimental and numerical analysis of single-lap joints for the automotive industry" *International Journal of Adhesion and Adhesives* 29 (4): 405-413.
- Gyeong-Seok Chae, Hee-Woong Park, Jung-Hyun Lee, Seunghan Shin 2020 "Comparative Study on the Impact Wedge-Peel Performance of Epoxy-Based Structural Adhesives Modified with Different Toughening Agents" *Polymers* 12, 1549; doi:10.3390/polym12071549.
- Higgins A. 2009. "Adhesive bonding of aircraft structures" *Int J Adhesion Adhesive* 20: 367-376, 10.1016/S0143-7496(00)00006-3.
- ISO 11343 – Adhesive. Determination of dynamic resistance of high-strength adhesive joints to separation under impact conditions – Wedge impact method.
- Komorek A., Godzimirski J. 2016 "The selected aspects of the research into impact loading of adhesive joints in block samples – comparison of different ways of applying the load" *Maintenance Problems* 103 (4): 77-91.
- Komorek A., Godzimirski J., Rośkiewicz M. 2020 "Analysis of new shape of test specimen for block shear impact test" *Materials* 13 1693, <https://doi.org/10.3390/ma13071693>.
- Komorek A., Godzimirski J. 2021 "Modified pendulum hammer in impact tests of adhesive, riveted and hybrid lap joints" *International Journal of Adhesion and Adhesives* 104, <https://doi.org/10.1016/j.ijadhadh.2020.102734>.
- Machado J.J.M., Marques E.A.S., Silva M.R.G., da Silva Lucas F.M. 2018 "Numerical study of impact behaviour of mixed adhesive single lap joints for the automotive industry" *International Journal of Adhesion and Adhesives* 84: 92-100.
- Raykhare S.L., Kumar P., Singh R.K., Parameswaran V. 2010 "Dynamic shear strength of adhesive joints made of metallic and composite adherents" *Material and Design* 31: 2102-2109.
- Rośkiewicz M, Godzimirski J., Komorek A., Jaształ M. 2021 "The Effect of Adhesive Layer Thickness on Joint Static Strength" *Materials*, 14 (6), 1499; <https://doi.org/10.3390/ma14061499>.
- da Silva L.F.M., Öchsner A., Adams R.D. (Eds.), *Handbook of adhesion technology*, Springer, Heidelberg 2011.
- Taylor A. 1996 Impact Testing of Adhesive Joints. *MTS Adhesive Project 2 AEA Technology*, 5 (2).

## HORIZONTAL LAMINAR FLOW CABINET WITH A LOW BACKGROUND AND CLEAN AIR

### POZIOMA KOMORA LAMINARNA Z NISKIM TŁEM I CZYSTYM POWIETRZEM

Tomasz SAMBORSKI<sup>1,\*</sup> , Andrzej ZBROWSKI<sup>1</sup> , Stanisław KOZIOL<sup>1</sup> 

<sup>1</sup> Łukasiewicz Research Network – Institute for Sustainable Technologies, Kazimierza Pułaskiego 6/10, 26-600 Radom, Poland

\* Corresponding author: [tomasz.samborski@itec.lukasiewicz.gov.pl](mailto:tomasz.samborski@itec.lukasiewicz.gov.pl)

#### Abstract

The publication presents the design, construction of a prototype, and the course of verification tests of a special horizontal laminar flow cabinet made entirely of plastics. In the cabinet design process, numerical simulations and airflow analyses were used to achieve a laminar, uniform flow in the device's workspace. A prototype was built and subjected to verification tests regarding the intensity and nature of airflow as well as air cleanliness. The cabinet is equipped with its own filtration-ventilation module providing clean air to the workspace and removing used air to the external ventilation system. It ensures an increased level of protection for workers dealing with microorganisms and hazardous airborne chemicals, as well as complete corrosion resistance inside the workspace. A particular area of application for the cabinet is research involving radionuclides, volatile, toxic chemical compounds for which air-recirculating devices cannot be used in the room where they are placed. The developed solution has been protected by industrial property rights and used to implement a contract for the supply of a set of equipment to the laboratory of the Institute of Nuclear Physics of the Polish Academy of Sciences.

**Keywords:** laminar flow cabinet, prototype, airflow testing

#### Streszczenie

Publikacja przedstawia projekt, budowę prototypu oraz przebieg badań weryfikacyjnych specjalnej komory laminarnej o poziomym przepływie powietrza wykonanej w całości z tworzyw sztucznych. W procesie projektowania komory wykorzystano symulacje numeryczne i analizy ruchu powietrza w celu uzyskania laminarnego ujednoczonego przepływu w przestrzeni roboczej urządzenia. Zbudowano prototyp i poddano badaniom weryfikacyjnym pod względem intensywności i charakteru przepływu oraz czystości powietrza. Komora jest wyposażona we własny moduł filtracyjno-wentylacyjny dostarczający czyste powietrze do przestrzeni roboczej oraz usuwający powietrze zużyte do systemu wentylacji zewnętrznej. Zapewnia zwiększony stopień ochrony pracowników zajmujących się pracą z drobnoustrojami oraz niebezpiecznymi lotnymi substancjami chemicznymi, a także całkowitą odporność na korozję wewnątrz przestrzeni roboczej. Szczególny obszar zastosowania komory stanowią badania z udziałem radionuklidów, lotnych, toksycznych związków chemicznych, w przypadku których nie wolno stosować urządzeń z recyrkulacją powietrza do pomieszczenia, w którym są ustawione. Opracowane rozwiązanie zostało objęte ochroną własności przemysłowej i wykorzystane do realizacji kontraktu na dostawę zestawu aparatury do laboratorium Instytutu Fizyki Jądrowej PAN.

**Słowa kluczowe:** komora laminarna, prototyp, badania przepływu powietrza

## 1. Introduction

Laminar flow cabinets are devices used in laboratory work requiring a sterile environment (Miring'u et al., 2017, Vellutato, 2021). In the

designated space of the cabinet, a unidirectional, laminar flow of sterile air occurs, with constant velocity and approximately parallel streamlines. The air is pre-filtered through a pre-filter and a HEPA filter. The purified air exits the cabinet in a continuous,



uniform stream, forming a barrier that impedes the entry of bacterial spores or fungal spores, which are constantly present in the air outside the cabinet (Barbosa et al., 2017, Parks et al., 2022). This allows for the maintenance of sterile conditions required for work, including with bacteria or cell cultures (Pawar

et al., 2021). Another application of laminar flow cabinets is to protect research personnel from the harmful effects of substances used during laboratory work conducted inside the cabinet. In terms of construction, there are cabinets with horizontal or vertical airflow (Fig. 1).

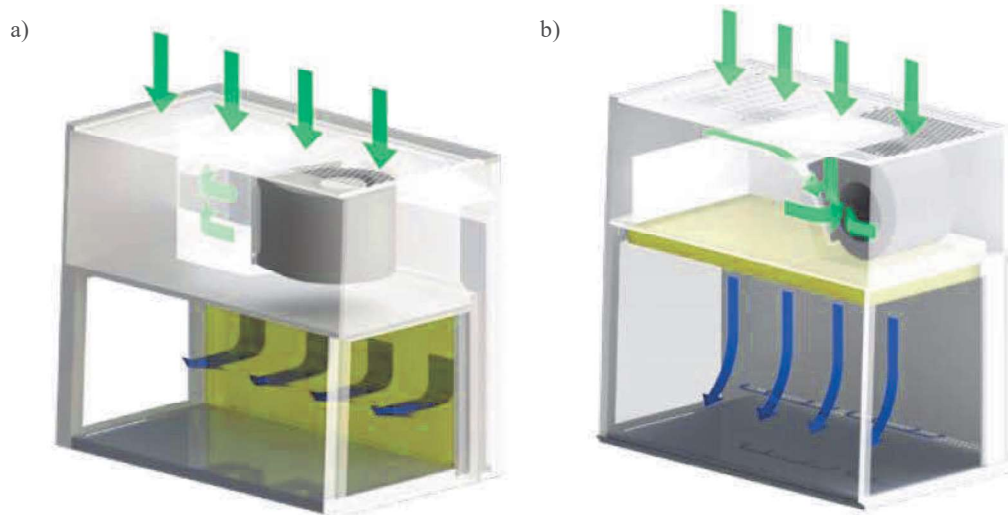


Fig. 1. Diagrams showing a) horizontal and b) vertical airflow in a laminar flow cabinet (Guide, 2024)

The criteria for the operation and classification of laminar flow cabinets intended for safe microbiological work are contained in the standard PN-EN 12469:2002. The standard distinguishes three classes of cabinets for safe microbiological work.

A class I cabinet with a large window in the front wall, through which the person working can perform tasks inside it, protects the worker and prevents the escape of contaminants generated inside the cabinet through the airflow, thanks to forced inward flow into the chamber and exhaust air filtration. It is suitable for work involving low or moderate-risk toxic agents where product (sample) protection is not required.

A Class II cabinet, with a similar construction, has additional air filtration circuits inside the chamber and exhaust air filtration. It provides protection for personnel, the environment, and the sample (Lapamnouyup et al., 2022, Jones et al., 2001). In a Class II cabinet, an internal unidirectional downward laminar airflow and an air curtain at the cabinet opening are used.

In a Class III cabinet, the workspace is completely enclosed. The person working is isolated from the workspace by a physical barrier (e.g., gloves). Filtered air is continuously supplied to the cabinet, and exhaust air is treated to prevent the release of microorganisms and chemical contaminants. In the workspace, a negative pressure of approximately 120 Pa is maintained, and airflow is forced by an external ventilation system.

Laminar flow cabinets are most commonly constructed from stainless steel with a front shield (glass or plastic), which either opens completely or allows the user's hands to be inserted into the workspace. Typical equipment in cabinets includes air/gas valves, electrical sockets, a sink, and a water tap (Vellutato, 2021).

The Łukasiewicz Institute for Sustainable Technologies has extensive experience in designing and manufacturing research equipment capable of achieving specific atmospheric parameters required for test environments (Kozioł, et al., 2019, Kozioł, et al., 2021, Samborski et al., 2022). Examples of such equipment include sets for testing volatile organic compound (VOC) emissions from building materials and wood, climate chambers with wide ranges of temperature and humidity changes, dust, aging, rain, corrosion, condensation, and calorimetric chambers. The experience and expertise gained during the execution of these projects enabled the achievement of the goal described in this work, which was the development and construction of a set of special laminar flow cabinets made entirely of plastics, following the requirements of the Institute of Nuclear Physics of the Polish Academy of Sciences. The most important requirements of the purchaser were to achieve laminar, horizontal airflow and air cleanliness delivered to the chamber in ISO6 class.

## 2. Laminar Flow Cabinet Design

The developed acid-resistant laminar flow cabinet with horizontal airflow direction in non-metallic execution is a niche product not offered on the market. Its unique design, characterized by the complete elimination of metallic elements from the workspace, prevents corrosion and increases the cabinet's opera-

tional durability. A specially designed laminarizer with appropriately distributed outlet holes organizes airflow and ensures a uniform horizontal flow. The possibility of collaboration with an exhaust system ensures the removal of hazardous vapors from the room while maintaining clean room requirements.

Figure 2 depicts a virtual 3D model of the constructed cabinet with horizontal laminar flow.

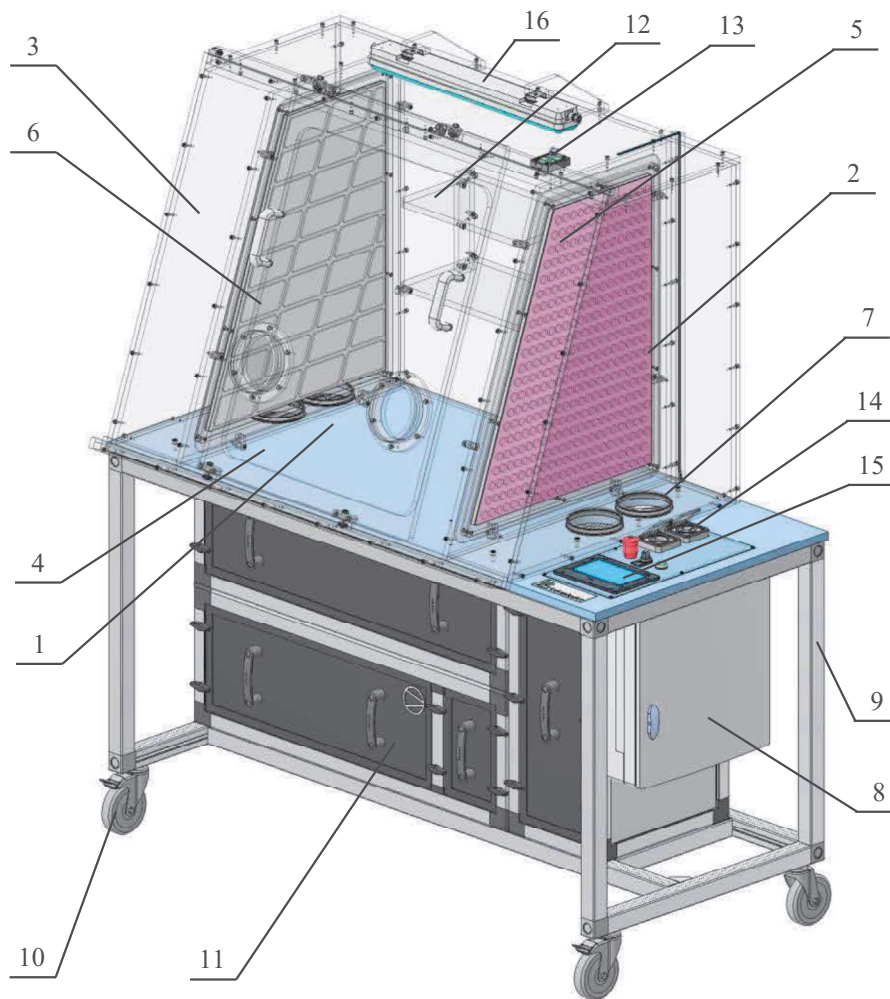


**Fig. 2.** 3D virtual model of the laminar flow cabinet (front view): 1 - workspace, 2 - inlet chamber, 3 - outlet chamber, 4 - sliding doors, 5 - inlet partition (right), 6 - outlet partition (left), 7 - inlet channels, 8 - control system cabinet, 9 - frame, 10 - caster wheel with lock, 11 - ventilation module, 12 - shelves, 13 - cable gland, 14 - power sockets, 15 - control panel, 16 - LED lighting

The laminar flow cabinet, constructed from PMMA panels, consists of three spaces:

- the central workspace 1, where laminar, horizontal airflow is achieved,
- the inlet chamber 2, supplied with filtered air from the ventilation module 11 through ducts 7,
- the outlet chamber 3, from which the air flows into the ventilation module and then to the discharge, where it is expelled outside (Fig. 3).

Between chambers 1, 2, and 3, there are partitions 5 and 6 made of perforated PMMA panels and

appropriately selected filter mats. The damping properties of the mats, perforation of the partitions, and the pressure and flow rate of the airflow are selected so that a laminar, orderly flow occurs horizontally in the workspace 1. Access to the interior of the cabinet is provided through sliding doors 4, which are designed with sockets for glove attachment. The lower wall of the airtight cabinet is the workbench. Inside the cabinet, there are two shelves 12, and a cable gland 13 is located in its upper wall. The cabinet, along with the workbench, is placed on

a mobile frame 9, housing the ventilation module 11 that implements the airflow circuit depicted in Figure 3. The electronic control system console 8 contains the device's control system with software, operated using the control panel 15. The workspace of the cabinet is

illuminated by an external LED lamp 16. Next to the control panel, electrical power sockets are installed for the optional powering of additional equipment used during experiments.

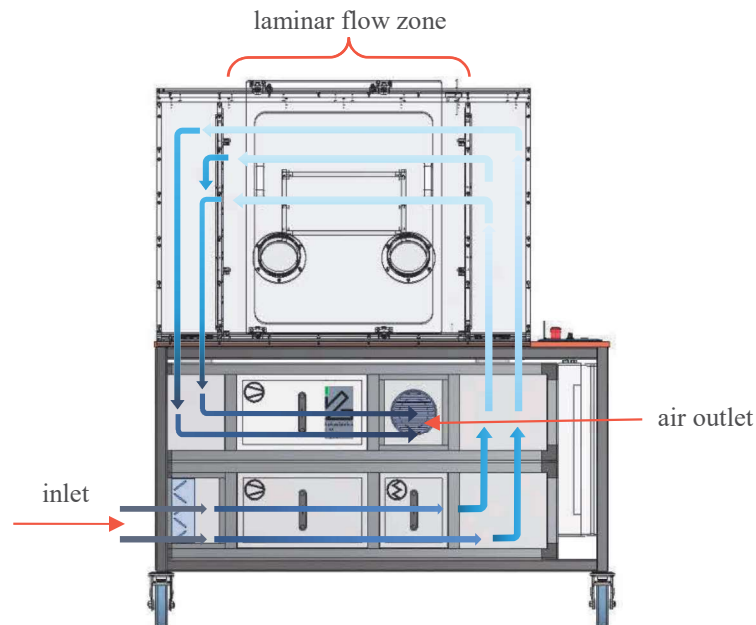


Fig. 3. Air circulation in the laminar flow cabinet

### 3. Airflow Simulations and Analyses

During the construction and refinement stages of the virtual spatial model and the development of the device's construction documentation, numerical simulations and airflow analyses were conducted. The aim was to preliminarily select airflow parameters and verify the model. The following parameters were adopted for the numerical calculations:

- Total airflow capacity through the device ranging from 100 to 300 m<sup>3</sup>/h.
- Flow with a capacity above 200 m<sup>3</sup>/h is used for intensive ventilation of the workspace and does not need to be laminar.
- The construction of partitions between the inlet, workspace, and outlet chambers can be modified (filling degree, shape of openings, type of filter mat) to optimize the flow distribution through the workspace.
- It is possible to divide the airflow streams supplied from the ventilation module to the inlet chamber and extracted from the outlet chamber (two flow channels each) and adjust the flow velocity in individual channels (typically achieved through the use of interchangeable baffles).

During the simulations, the flow resistance through the partitions, division of airflow streams, and

flow velocities in the channels connecting the chambers to the ventilation module were varied.

The calculations were performed using computational fluid dynamics (CFD) software - Autodesk<sup>®</sup> CFD, which is a tool used to solve equations describing fluid flow using numerical methods. The use of such tools provides extensive capabilities for analyzing flow phenomena and processes, enables a better understanding of them, and thus allows for the optimization of existing solutions. During the development of new products, CFD is used as a tool to shorten the product development time.

During the simulation process, constant volumetric flow conditions at the inlet and outlet of the chamber were assumed as boundary conditions. The analysis concerned calculations excluding the temperature change and impact to achieve a steady-state flow condition. The model was meshed using adaptive technology, starting with default settings for the density of finite element mesh with initial three wall-adjacent layers and a gradation factor of 0.45. A modified Petrov-Galerkin method was used as a computational model (advection scheme) to ensure stability of calculations. Air with constant parameters was used as an agent (Table 1).

**Table 1.** Air parameters used in the CFD analysis

Material Environment			
<input checked="" type="radio"/> Fixed <input type="radio"/> Variable			
<input checked="" type="checkbox"/> Use scenario environment			
Properties for Air (fixed) Environment: 101325 Pa, 19.85 Celsius (from scenario)			
Property	Value	Units	Underlying variation
Density	1,20473e-06	g/mm3	Equation of State
Viscosity	1,817e-05	Pa-s	Constant
Conductivity	2,563e-05	W/mm-K	Constant
Specific heat	1,004	J/g-K	Constant
Cp/Cv	1,4	none	Constant
Emissivity	1	none	Constant
Wall roughness	0	millimeter	Constant
Phase	0		Vapor Pressure

Figures 4 and 5 show the results of the calculations in graphical form showing the flow velocity distributions, directions and distribution of air flows for a total flow through the cabinet equal to 150 m<sup>3</sup>/h. An ordered flow through the workspace in a horizontal direction with a constant velocity distribution across the entire cross-section of the cabinet, excluding the wall areas, is visible.

From Figure 4b, it can be inferred that the expected airflow pattern was achieved by supplying the inlet chamber from one of the two ducts connecting it to the ventilation module and by extracting air from the outlet chamber through both modeled ducts. The results of the numerical calculations were used to develop the design of the partitions and to select the interaction mode of the cabinet with the ventilation module. The results were verified during prototype testing.

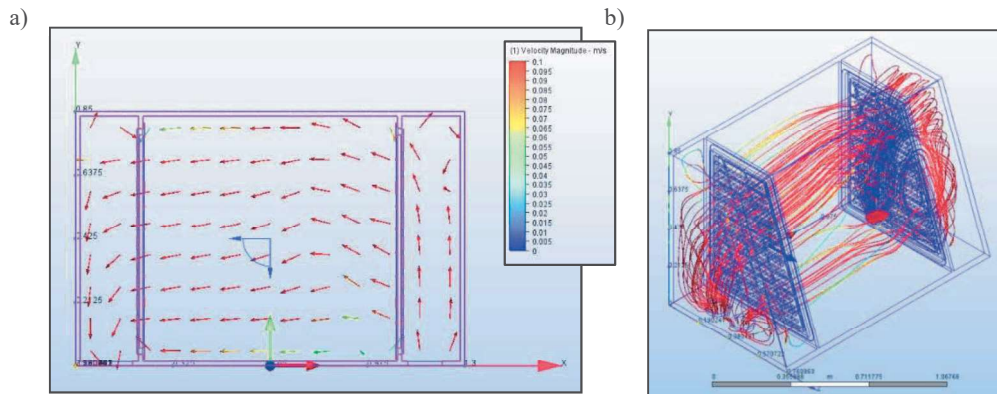


**Fig. 4.** The result of the airflow simulation in the cabinet: a) velocity distribution in the inlet, workspace, and outlet chambers, b) airflow distribution (view from the outlet chamber side)

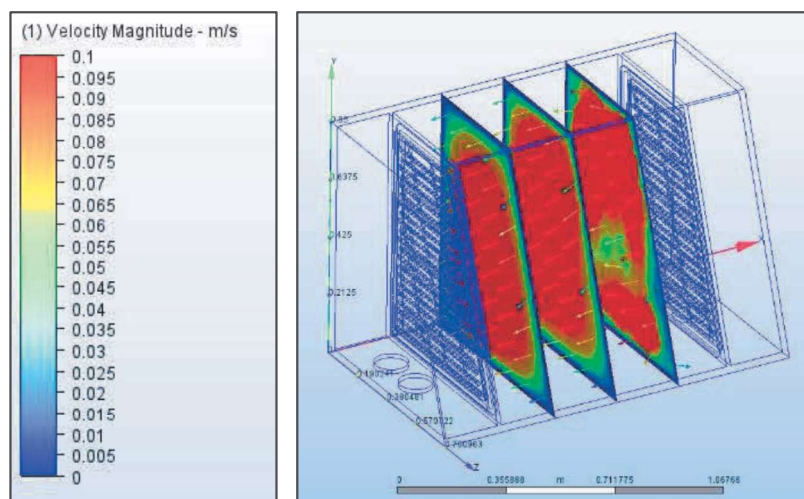


**Fig. 5.** Result of airflow simulation in the cabinet – velocity distribution in the workspace in selected vertical planes

#### 4. Prototype and Verification Testing of the Special Laminar Flow Cabinet

The prototype of the special laminar flow cabinet was manufactured at the Łukasiewicz – ITEE Prototyping Center based on the developed technical documentation. Most of the structural elements in contact with the internal experimental environment were made of polymethyl methacrylate (PMMA) sheets joined by polyamide screw connectors. Such a design, according to the assumptions, prevents corrosive processes that may occur during work with aggressive chemical environments. Figure 6 shows a photograph of the prototype cabinet.



Fig. 6. Prototype laminar flow cabinet made of plastic

The control of all functions of the complete device is performed using the operator's panel. Most control functions are accessible from the touch control panel equipped with user software (Fig. 7). The operator menu allows for adjustment and displays values of the airflow rate through the cabinet and the pressure difference relative to the surroundings. It is used to stabilize device operating parameters and signal warning and failure states, such as filter clogging or fan damage.

The constructed prototype of the cabinet was started up and tested to perform all manual and automatic operational activities.

The prototype underwent verification testing to ensure that the technical parameters of the device met the customer's requirements. The tests included the following:

- measurement of the airflow rate through the cabinet,

- examination of the airflow velocity distribution,
- examination of air cleanliness,

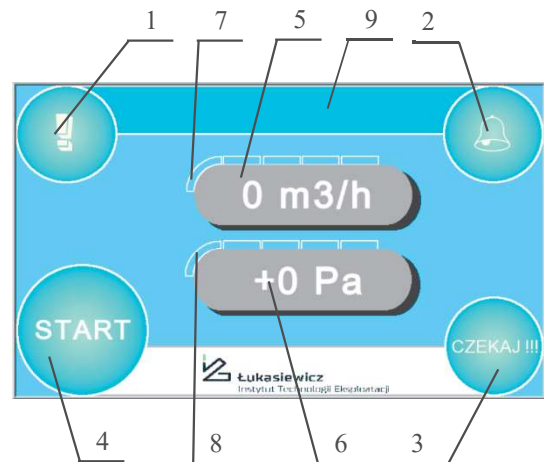


Fig. 7. View of the control panel: 1 - warning icon, 2 - alarm icon, 3 - ready-to-operate icon, 4 - device activation icon, 5 - information about current airflow rate, 6 - information about current pressure difference between the cabinet and the surroundings, 7 - barograph of the percentage efficiency of the supply fan, 8 - barograph of the percentage efficiency of the exhaust fan, 9 - field with information about alarms, warnings, and current events

The airflow rate through the cabinet ranging from 100 to 400 m<sup>3</sup>/h was measured under normal conditions using a balometer, with a measurement uncertainty of  $\pm 3\%$  of the measured value, and compared with the indications on the operator panel calculated based on the measured pressure difference at the fan and its characteristic. In the range of airflow rates up to 200 m<sup>3</sup>/h, the relative measurement error was up to 7%, while above this range, it did not exceed 4%. The exact value of the airflow rate through the cabinet is not a critical parameter of the process being carried out and serves to assess the intensity of its ventilation. Therefore, the achieved measurement accuracy is sufficient.

Local airflow velocity measurements inside the chamber were conducted at nodes defined by a grid of measurement points evenly distributed across the transverse middle section of the workspace. Table 2 shows the coordinates of each measurement point and the measured airflow velocity values at those points.

**Table 2.** Airflow velocity distribution in m/s in the central plane of the chamber for an airflow rate of 300 m<sup>3</sup>/h

Y-coordinate of the measurement point [mm]	727	0.08	0.14	0.17	0.26	0.17				
	666	0.00	0.16	0.24	0.23	0.23	0.10			
	604	0.02	0.07	0.14	0.22	0.25	0.19			
	533	0.00	0.19	0.25	0.23	0.37	0.23			
	462	0.17	0.19	0.22	0.21	0.32	0.16	0.10		
	373	0.19	0.23	0.31	0.20	0.20	0.26	0.23		
	302	0.23	0.30	0.33	0.19	0.21	0.23	0.21	0.17	
	231	0.24	0.20	0.25	0.18	0.21	0.30	0.30	0.05	
	169	0.21	0.16	0.16	0.27	0.20	0.18	0.33	0.19	
	108	0.19	0.28	0.22	0.29	0.24	0.21	0.35	0.23	0.31
		107	169	230	290	351	412	472	533	595
		X-coordinate of the measurement point [mm]								

The Y-coordinate of the measurement point represents its distance from the chamber's bottom surface (table), while the X-coordinate represents its distance from the rear wall. Measurements were performed using a thermo-anemometer probe with a measurement uncertainty of ± 0.015 m/s. The

measurement results indicate a sufficiently uniform velocity distribution in the central transverse plane of the chamber, except for the wall areas where the velocity is lower than the average value. In Table 3, the average values of laminar airflow velocity are shown for several selected total airflow rates.

**Table 3.** Average values of laminar airflow velocity in the cabinet for selected total airflow rates

Airflow rate through the cabinet [m <sup>3</sup> /h]	150	200	300
Average value of air velocity in the working chamber [m/s]	0.09 ±0.048	0.13 ±0.055	0.21 ±0.076

The laminar airflow character in the working chamber was also confirmed using a smoke test according to the method described in the PN-EN ISO 14644-3 standard, section B.3 – the introduction of a marker (smoke generated from test tubes containing smoldering sulfuric acid) into the air stream (Fig. 8).

Air cleanliness in the working chamber was assessed using the particle counter Met One 3423

(Fig. 9a) (flow rate of the counter: 50 l/min., measurement channels from 0.3 to 10 μm, measurement uncertainty ISO-21501-4 Calibration). The test was conducted under the same conditions as the other verification tests.

Figure 9b shows the particle counter during measurements in the cabinet and the test report with a total airflow rate of 300 m<sup>3</sup>/h.



**Fig. 8.** Airflow smoke test

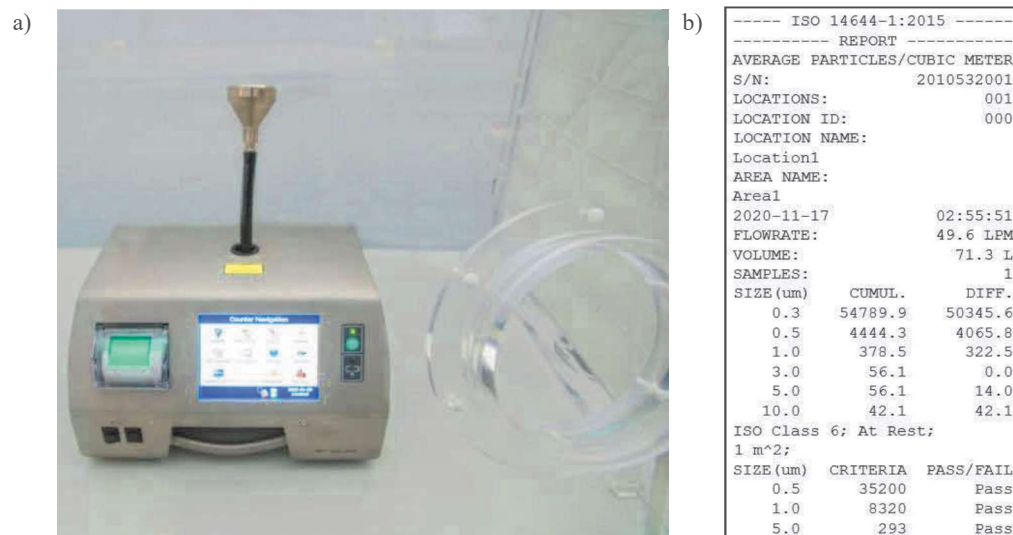


**Fig. 9.** Air cleanliness test in the working chamber using the particle counter Met One 3423 (a), and the test report for a total airflow rate of 300 m<sup>3</sup>/h (b)

The functional tests of the prototype laminar flow cabinet and the results of the verification tests confirmed that the constructed device meets the technical and functional requirements formulated during the conceptualization and technical design stage.

## 5. Summary

At Łukasiewicz – ITEE in Radom, a prototype laminar flow cabinet with horizontal airflow, entirely made of plastics, was developed and constructed. The concept and operation of the device were developed in cooperation with and commissioned by the Institute of Nuclear Physics of the Polish Academy of Sciences. During the device's design, numerical simulations and airflow analyses were utilized to achieve the required laminar horizontal airflow throughout the working chamber's volume. A fully functional prototype chamber equipped with purification and ventilation module was built and subjected to comprehensive verification testing within a complete laboratory setup. The developed chamber allows for collaboration with an external exhaust system and provides complete corrosion resistance inside the working space. The combination of these features makes it a unique product not previously available on the market. A set of four chambers was manufactured and installed in the laboratory of the Institute of Nuclear Physics of the Polish Academy of Sciences in Kraków. The original design solutions developed at Łukasiewicz – ITEE have been protected by industrial design registration (Rp.27206, 2021).

Further work is planned to increase the functionality of the device. This includes equipping the chamber with a water supply and sewerage system

(sink, eye wash station), and consequently modifying the structure of the ventilation module.

## References

- Barbosa, B. P. P., & Brum, N. D. C. L. (2017). Sensitivity tests of biological safety cabinets' contaminant contention to variations on indoor flow parameters in biosafety level laboratories. *Building and Environment*, 124, 1-13.
- A Guide to Biosafety & Biological Safety Cabinets, Esco Lifesciences, <https://www.escolifesciences.com>, (dostęp 16.04.2024).
- Jones, R. L., & Eagleson, D. (2001). Ergonomic considerations in the development of a class II, type A/B3 biological safety cabinet. *American clinical laboratory*, 20(4), 37-42.
- Kozioł S., Matecki K., Samborski T., Siczek M., Wojutyński J., Zbrowski A. 2019. Overpressure chamber for testing in high air purity conditions. *Journal of Machine Construction and Maintenance* (3): 81-90
- Kozioł S., Samborski T., Siczek M., Zbrowski A. 2021. System for testing resistance for static exposure to dust. *Technologia i automatyzacja montażu* (4): 24-28.
- Lapamnouyup, A., Ganjanasiripong, P., Kaewpan, A., & Chuen-im, T. (2022). Comparative study of product contamination rates in class II biological safety cabinets with and without ultraviolet light disinfection. *Science, Engineering and Health Studies*, 22030004-22030004.
- Miring'u, G., Bundi, M., Muriithi, B. K., Apondi, E. W., Galata, A. A., Kathiiko, C. N., ... & Ichinose, Y. (2017). Knowledge and practices regarding usage of biological safety cabinets. *Applied Biosafety*, 22(1), 38-43.
- Parks, Simon & Hookway, Helen & Kojima, Kazunobu & Bennett, Allan. (2022). The Impact of Air Inflow and Interfering Factors on the Performance of Microbiological Safety Cabinets. *Applied biosafety: journal of the American Biological Safety Association*. 27. 23-32. 10.1089/apb.2021.0010.
- Pawar, S. D., Khare, A. B., Keng, S. S., Kode, S. S., Tare, D. S., Singh, D. K., & Mullick, J. (2021). Selection and

- application of biological safety cabinets in diagnostic and research laboratories with special emphasis on COVID-19. *Review of Scientific Instruments*, 92(8).
- Rp.27206. 2021. Komora laminarna.
- Samborski T., Zbrowski A., Koziol S. 2022. Test system to verify thermal shock resistance. *Technologia i automatyzacja montażu* (2): 24-31.
- Vellutato, A. (2021). Cleaning and Disinfecting Laminar Flow Workstations, Bio Safety Cabinets and Fume Hoods. In *Handbook of Validation in Pharmaceutical Processes*, Fourth Edition (pp. 419-428). CRC Press.

## ACCURACY OF ASSEMBLY HOLES AFTER DRILLING IN AL/CFRP LAYERED STRUCTURE

### DOKŁADNOŚĆ WYKONANIA OTWORÓW MONTAŹOWYCH PO WIERCENIU KONSTRUKCJI WARSTWOWEJ TYPU AL/CFRP

ElŹbieta DOLUK<sup>1,\*</sup> , Izabela MITURSKA-BARAŃSKA<sup>1</sup> ,  
Oleksandra KRUPOVYCH<sup>1</sup>

<sup>1</sup> Department of Production Computerisation and Robotisation, Faculty of Mechanical Engineering, Lublin University of Technology, Nadbystrzycka 36, 20–618 Lublin, Poland

\* Corresponding author: e.doluk@pollub.pl, tel.: (+48) 507 666 485

#### Abstract

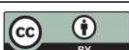
Layered structures consisting of CFRP composites and aluminum alloys are most commonly used in the aerospace, marine, construction and automotive industries. One of the most important aspects associated with their use is the difficulty of machining them due to the anisotropic nature of the structures. These structures are often jointed to each other by mechanical joints that require mounting holes. The purpose of this study was to determine the effect of drill bit diameter, cutting speed and the way the specimen is clamped during machining (drilling strategy) on the quality of holes drilled in a II-layer structure consisting of CFRP composite and aluminum alloy. The quality of the holes was expressed by the hole accuracy index D. A visual evaluation of the holes after the drilling process was also carried out. The most accurate holes (the lowest value of the hole accuracy index D) were obtained at the exit of the drill bits with  $\varnothing 4$  mm and  $\varnothing 8$  mm diameters, a cutting speed of  $v_c = 90$  m/min and an Al/CFRP drilling strategy. The lowest dimensional accuracy of the hole was also obtained at the exit of the drill bit, but using a cutting tool with a diameter of  $\varnothing 6$  mm, a cutting speed of  $v_c = 30$  m/min and an Al/CFRP drilling strategy. The values of the D index and visual evaluation of the holes also made it possible to note that for this type of material it is more favorable, considering the dimensional accuracy of the holes, to use a CFRP/Al drilling strategy.

**Keywords:** drilling, Al/CFRP stacks, assembly holes, cutting parameters

#### Streszczenie

Konstrukcje warstwowe składające się z kompozytów CFRP i stopów aluminium są najczęściej stosowane w przemyśle lotniczym, morskim, budowlanym oraz motoryzacyjnym. Jednym z najważniejszych aspektów związanych z ich zastosowaniem jest trudność ich obróbki wynikająca z anizotropowości konstrukcji. Konstrukcje te są często łączone ze sobą za pomocą połączeń mechanicznych, które wymagają wykonania otworów montażowych. Celem niniejszej pracy było określenie wpływu średnicy wiertła, prędkości skrawania i sposobu zamocowania próbki podczas obróbki (strategia wiercenia) na jakość otworów wykonywanych w II warstwowej konstrukcji składającej się z kompozytu CFRP i stopu aluminium. Jakość otworów wyrażono za pomocą wskaźnika dokładności wykonania otworu D. Przeprowadzono także ocenę wizualną otworów po procesie wiercenia. Najdokładniejszy otwór (najmniejszą wartość wskaźnika D) otrzymano na wyjściu otworów z wykorzystaniem wiertel o średnicach  $\varnothing 4$  mm i  $\varnothing 8$  mm, prędkości skrawania  $v_c = 90$  m/min oraz strategii wiercenia Al/CFRP. Najmniejszą dokładność wymiarową otworu uzyskano również na wyjściu narzędzia, jednak z zastosowaniem wiertła o średnicy  $\varnothing 6$  mm, prędkości skrawania  $v_c = 30$  m/min i strategii wiercenia Al/CFRP. Otrzymane wartości wskaźnika D oraz ocena wizualna pozwoliły zauważyć także, że dla tego typu materiałów korzystniejszym rozwiązaniem, biorąc pod uwagę dokładność wymiarową otworów, jest zastosowanie strategii wiercenia CFRP/Al (wejście narzędzia skrawającego w warstwę kompozytową, wyjście wiertła w warstwie metalowej).

**Słowa kluczowe:** wiercenie, konstrukcje warstwowe Al/CFRP, otwory montażowe, parametry skrawania



## 1. Introduction

One of the basic machining processes applied to heterogeneous materials, which include layered materials that are a combination of metal and polymer matrix composite, is the drilling process. Drilling holes in such structures is an important step in their assembly process – holes can be used to attach auxiliary units (e.g., bolts, rivets), introduce assembly components (e.g., adhesives, clamps, bushings) or carry out other assembly operations (Kausar et al., 2023). Layered materials are used in many industries due to their mechanical and physical properties, including light weight, bending and shear strength, ability to carry heavy loads, and impact resistance (Hosseinkhani et al., 2024). Performing the drilling process in structures that are a combination of materials with very different properties is a major challenge (Changze et al., 2023). Therefore, it is necessary to adapt the machining conditions to the specifics of the materials to ensure the desired surface quality after machining. This can be achieved by using appropriate cutting tools and cutting parameters (Kilickap, 2020).

When drilling holes in sandwich structures consisting of aluminum alloy and CFRP (Carbon Fibre Reinforced Plastic) composite having abrasive fibers in its structure, various problems may arise due to the specific structure and properties of the material so formed. The anisotropic structure of fiber composites is the main factor that has a significant impact on their strength, but on the other hand it makes the process of their processing largely difficult (Zhang et al., 2020). Difficulties in obtaining holes with reproducible dimensional and shape accuracy, excessive cutting tool wear, the occurrence of typical machining defects such as delamination, fiber pullout, matrix cracking, undercut fibers, and frayed edges at the entrance and exit of the cutting tool are examples of phenomena that can occur when drilling holes in CFRP composites and layered materials formed on their basis (Cieciela, 2022). The main phenomenon that hinders the process of drilling holes in this type of structures is delamination, which leads to a loss of cohesion of the individual layers of the CFRP composite and the entire layered structure (Ergün et al., 2021). An enlargement of the delamination area can occur even when the cutting edges of the tools are slightly dulled. Delamination during drilling can occur at the entrance and exit of the drill bit from the workpiece material. In the entry zone, delamination is characterized by the winding of carbon fibers on the drill bit and their tearing before the material is removed. In the exit zone, delamination occurs as a result of the lower layers of the composite being pushed out and separated from the remaining fibers (Isbilir et al., 2013). Delamination

can lead to damage to the integrity of the structure and a reduction in strength. Studies have shown that proper adjustment of drilling conditions (rotational speed, cutting force and tool cooling system) can effectively reduce the risk of material delamination (Melentiev et al., 2016). In addition, improperly selected cutting tools, such as the use of brittle or vulnerable tool materials, can lead to the formation of micro-cracks in the surfaces, which reduces its strength and reduces the quality of the hole finish (Natarajan, et al., 2022; Alagan et al., 2023.).

A significant number of holes made in sandwich structures are assembly holes. After machining, the quality of the holes is often defined by the presence of defects on the machined surfaces. Delamination occurring between the inner layers, is caused by the tool passing through different cutting resistances (Yang et al., 2024). This type of delamination is a hidden material defect and is particularly dangerous from the point of view of structural safety. A significant problem that can be encountered when drilling metal-polymer composite layered materials is the insufficient quality of the machined hole, which can lead to difficulties in the assembly of structural components or a reduction in the aesthetics of the final product. A review of the literature indicates that the use of tools with appropriate geometries, such as rake angle and blade geometry, can significantly improve the quality of the hole (Isbilir et al., 2013; Saoudi et al., 2018).

The purpose of this study was to determine the effect of drill bit diameter, cutting speed and the way the specimen is clamped during machining (drilling strategy) on the quality of holes drilled in a II-layer structure consisting of CFRP composite and aluminum alloy. The work is a continuation of research conducted on the machinability and quality of holes drilled in layered structures.

## 2. Materials and methods

The subject of the study was a II-layer metal-polymer composite structure. The shape and dimensions of a spacement are shown in Fig. 1.

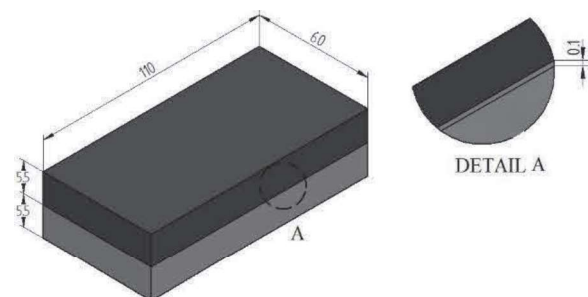


Fig. 1. Geometry and shape of the sample

The experiment investigated the effect of machining conditions on the dimensional accuracy of holes after the drilling process. Fig. 2 shows a diagram of the experiment conducted.

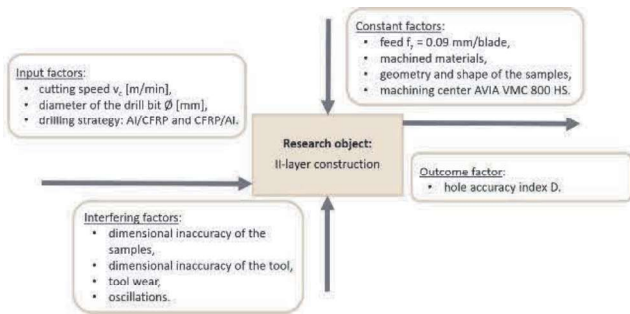


Fig. 2. Plan of the experiment

The structure consisted of two materials: a CFRP composite and an EN AW-2024 T3 aluminum alloy. The materials were chosen because of their frequent use in the aerospace and automotive industries. The layers were joined using an adhesive process. The characteristics and properties of the materials used and details of the bonding process are given in (Doluk, 2023).

The experiment examined the effects of cutting speed, drill bit diameter and drilling strategy on the dimensional accuracy of holes after the drilling process. The test was conducted using an AVIA VMS 800HS vertical machining center. The drilling process was carried out without the use of coolant due to the nature of the material to be machined (CFRP). The machining scheme is shown in Fig. 3.

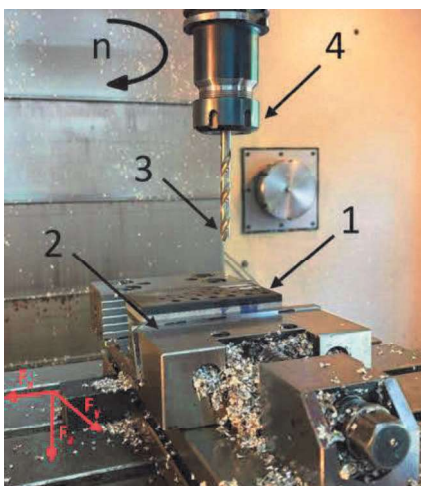


Fig. 3. Diagram of the drilling process: 1 – workpiece, 2 – machine vise, 3 – tool, 4 – spindle

Drill bits with diameters of  $\phi 8$  mm,  $\phi 6$  mm and  $\phi 4$  mm were used in the study. The manufacturer of the tools used is Kennametal. The drills were made of tungsten carbide and coated with TiAlN (*Titan*

*Aluminum-Nitride*) tool coating. This coating has good resistance to large temperature ranges, which allows machining with high cutting speeds.

Two machining strategies were adopted in the study:

- drilling of holes in the II-layer aluminum alloy type structure EN AW-2024 T3 composite CFRP, where the entry layer is aluminum alloy (Al/CFRP) (Fig. 4a),
- drilling holes in a II-layer CFRP-aluminum alloy EN AW-2024 T3 composite structure, where the entry layer is CFRP composite (CFRP/Al) (Fig. 4b).

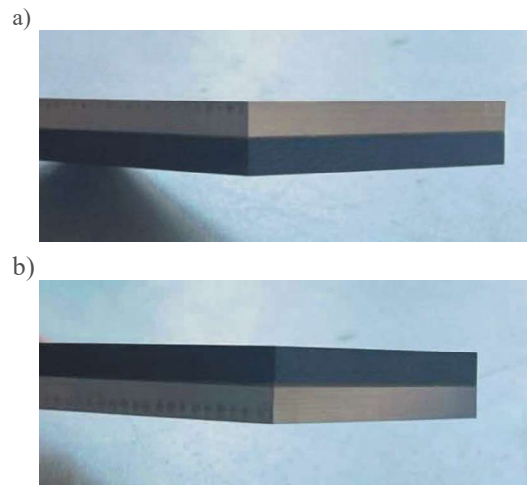


Fig. 4. Adopted drilling strategies: a) Al/CFRP strategy, b) CFRP/Al strategy

The values of the independent variables considered in this research are shown in Table 1. The study used a static, determined complete plan (PS/DC).

Table 1. Independent variables adopted in the experiment

Variable	Value		
Cutting speed $v_c$ [m/min]	30	60	90
Drill bit diameter [mm]	$\phi 8$	$\phi 6$	$\phi 4$
Drilling strategy	Al/CFRP	CFRP/Al	

The diameters of the treated holes were measured using a Keyence VHX-500 digital microscope. This device allowed recording the image with high accuracy (0.001). The dimensional accuracy of the holes was measured for all adopted machining variants at the entry and exit of the drill bit from the workpiece material. To determine the dimensional accuracy of the holes, the value of the hole accuracy index D was determined from the ratio of the arithmetic mean of the actual hole diameters  $D_{rz}$  obtained after machining and the nominal value of the hole in question. Hole diameters were measured using the Keyence VHX-

500 digital microscope. The quality of the machined holes was determined by the hole:

$$D = \left| 1 - \frac{D_{rz}}{D_N} \right| \tag{1}$$

where:  $D$  – hole accuracy index,  $D_{rz}$  – diameter of the hole after machining [mm],  $D_N$  – nominal diameter of the hole [mm].

The hole accuracy index  $D$  was assimilated to 0 – values closer to this digit indicated better dimensional accuracy of the hole. Each machining variate was performed three times to average the obtained diameter values, while each hole was expressed as the arithmetic average of three measurements.

When machining structures, comparing machining effects by dimensional accuracy alone may not be sufficient. It is also necessary to determine the condition of the hole edges. For this purpose, the holes were visually evaluated using the Keyence VHX-500 digital microscope with 100x magnification.

### 3. Results and discussion

Figures 5–10 show the effect of the tested machining conditions on the values of the hole accuracy index  $D$  at the entry and exit of the cutting tool.

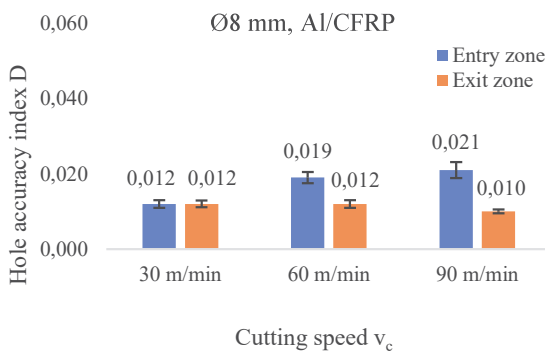


Fig. 5. Hole accuracy index  $D$  at the entry and exit of the cutting tool using Al/CFRP drilling strategy and drill bit diameter Ø8 mm

The maximum value of the  $D$  index (0.021) obtained after machining with the drill bit diameter Ø8 and the Al/CFRP drilling strategy was obtained at the entry of the cutting tool for the cutting speed of  $v_c = 90$  m/min, while the minimum value (0.010) was obtained at the exit of the drill bit and the same cutting speed (Fig. 5). In the above case, higher values of the  $D$  index were observed at the entry of the cutting tool, indicating poorer hole accuracy than at the exit of the drill bit. Analyzing the above data, it can be observed that the values of the  $D$  index at the entry of the tool increased with an increase in the cutting speed  $v_c$ , while at the exit of the drill bit they remained at the

same level or decreased with an increase in the cutting speed  $v_c$ .

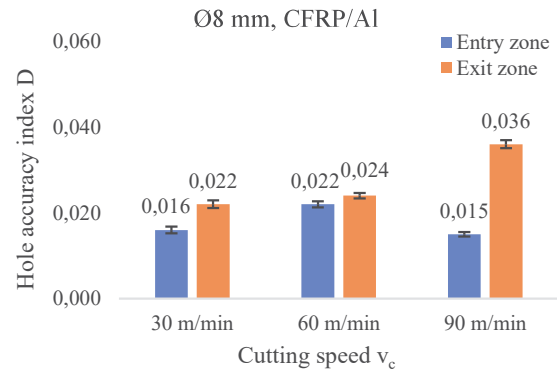


Fig. 6. Hole accuracy index  $D$  at the entry and exit of the cutting tool using CFRP/Al drilling strategy and drill bit diameter Ø8 mm

In the case of using the drill bit diameter Ø8 mm and the CFRP/Al drilling strategy (Fig. 6), the lowest value of the  $D$  index (0.015) was obtained at the entry of the cutting tool when using a cutting speed of  $v_c = 90$  m/min. The highest value of the hole accuracy index  $D$  (0.036) for the adopted cutting conditions was obtained at the cutting speed  $v_c = 90$  m/min at the exit of the cutting tool. The values of the  $D$  index obtained at the entry of the drill bit were equal to or higher than the values of the  $D$  index obtained at the exit of the cutting tool. Increasing the cutting speed in this case caused an increase in the value of the  $D$  index at the exit of the cutting tool.

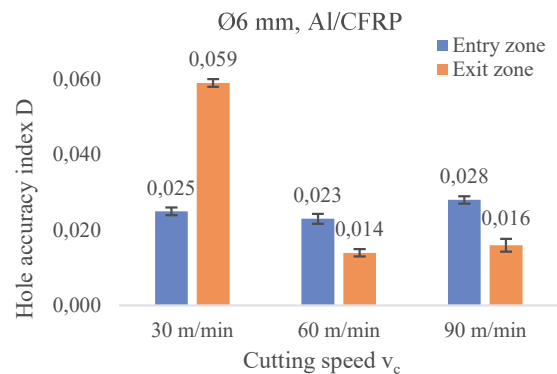
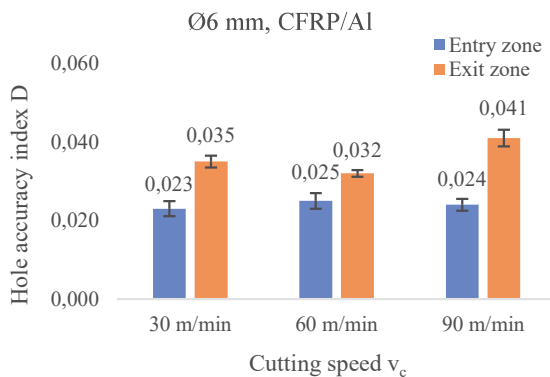


Fig. 7. Hole accuracy index  $D$  at the entry and exit of the cutting tool using Al/CFRP drilling strategy and drill bit diameter Ø6 mm

Fig. 7 shows the obtained results of the  $D$  index for the drill bit diameter Ø6 mm and the Al/CFRP drilling strategy. The highest value of the considered index (0.059) was obtained at the exit of the drill bit when using the cutting speed of  $v_c = 30$  m/min. The lower value of the hole accuracy index  $D$  (0.014), and therefore the highest dimensional accuracy, was also observed at the exit of the cutting tool, but using the cutting speed of  $v_c = 60$  m/min. Lower values of the  $D$

index were obtained at the exit of the cutting tool compared to the entry of the drill bit, except when using the lowest cutting speed, where the maximum value of the D index was obtained.



**Fig. 8.** Hole accuracy index D at the input and output of the cutting tool using CFRP/Al drilling strategy and drill bit diameter Ø6 mm

In Fig. 8 were presented the values of the hole accuracy index D for the drill bit diameter Ø6 mm and the CFRP/Al drilling strategy. The maximum value of the hole accuracy index D (0.041) was obtained at the exit of the cutting tool when using the cutting speed of  $v_c = 90$  m/min, while the minimum value of the index D (0.023) was obtained at the entry of the drill bit for the cutting speed of  $v_c = 30$  m/min. Comparing the results, it can be seen that the higher values of the D index were obtained at the exit of the cutting tool.

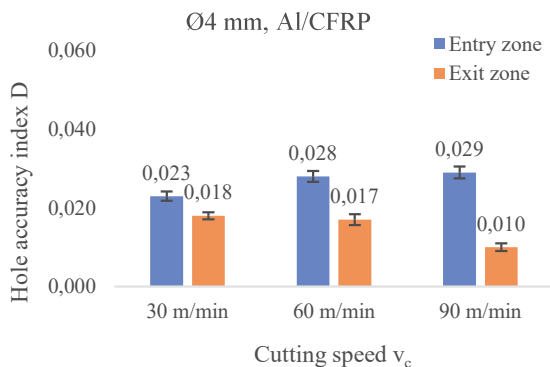


**Fig. 9.** Hole accuracy index D at the input and output of the cutting tool using Al/CFRP drilling strategy and drill bit diameter Ø4 mm

Analyzing Fig. 9, which presents the values of the hole accuracy index for the drill bit diameter Ø4 mm and the Al/CFRP drilling strategy, it is noted that for cutting speed  $v_c = 90$  m/min, the lowest value of the hole accuracy index D (0.010) was obtained at the exit of the cutting tool, while the highest value (0.029) was obtained at the entry of the drill bit. Higher values of the D index were obtained at the entry of the cutting

tool. Increasing the cutting speed in the analyzed case resulted in an increase in the value of the D index at the entry of the tool and a decrease in its value at the exit of the drill bit.

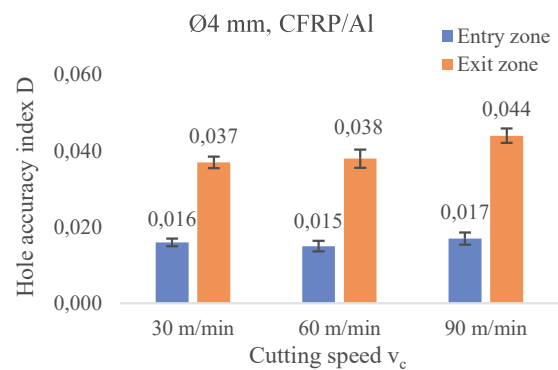


**Fig. 10.** Hole accuracy index D at the input and output of the cutting tool using CFRP/Al drilling strategy and drill bit diameter Ø4 mm

Considering the values of the hole accuracy index D obtained for the drill bit diameter Ø4 mm and the CFRP/Al drilling strategy (Fig. 10), it can be seen that the lowest value of the index D (0.015) was obtained at the entry of the drill bit at a cutting speed of  $v_c = 60$  m/min, while the highest value was obtained at the exit of the tool using a cutting speed of  $v_c = 90$  m/min. For all the considered cutting speeds, higher values of the D index were obtained at the exit of the cutting tool. For most of the results obtained, an increase in cutting speed resulted in an increase in the hole accuracy index D.

In order to determine the influence of individual input factors (cutting speed  $v_c$ , drill bit diameter  $\varnothing$  and the drilling strategy S) and their interactions ( $v_c \times \varnothing \times S$ ,  $v_c \times \varnothing$ ,  $v_c \times S$  and  $\varnothing \times S$ ) on the dimensional accuracy of the machined holes, a multivariate analysis of variance (ANOVA) was conducted at the significance level of  $\alpha = 0.05$ . Table 2 and Table 3 show the results of the statistical analysis.

**Table 2.** Three-factor ANOVA analysis of variance for the hole accuracy index D at the entry of the drill bit

Source	SS	DF	MS	F	<i>p-value</i>
$v_c$	0.004	2	0.002	5	0.024
$\varnothing$	98.652	2	49.326	146792	<0.001
S	0.002	1	0.002	7	0.017
$v_c \times \varnothing$	0.004	4	0.001	3	0.064
$v_c \times S$	0.002	2	0.001	4	0.039
$\varnothing \times S$	0.004	2	0.002	5	0.022
$v_c \times \varnothing \times S$	0.002	4	<0.001	1	0.249

**Table 3.** Three-factor ANOVA analysis of variance for the hole accuracy index D at the exit of the drill bit

Source	SS	DF	MS	F	<i>p-value</i>
$v_c$	0.012	2	0.006	0.7	0.491
$\emptyset$	98.182	2	49.091	5778.7	<0.001
S	0.073	1	0.073	8.6	0.009
$v_c \times \emptyset$	0.040	4	0.010	1.1	0.375
$v_c \times S$	0.038	2	0.019	2.3	0.131
$\emptyset \times S$	0.012	2	0.006	0.7	0.488
$v_c \times \emptyset \times S$	0.024	4	0.006	0.7	0.619

Based on the data presented in the tables, it can be seen that the dimensional accuracy of the holes at the entry of the cutting tool was most influenced by the drill bit diameter ( $F = 146792$ ;  $p\text{-value} < 0.001$ ). The interaction of all three independent variables ( $v_c \times \emptyset \times S$ ), like the interaction of  $v_c \times \emptyset$ , did not statistically affect the values of the index D. At the exit of the cutting tool, only two variables influenced the dependent variable: the drill bit diameter ( $F = 5779.7$ ;  $p\text{-value} < 0.001$ ) and the drilling strategy ( $F = 8.6$ ;  $p\text{-value} = 0.009$ ). The other factors had no effect from a statistical point of view on the obtained values of the hole accuracy index D.

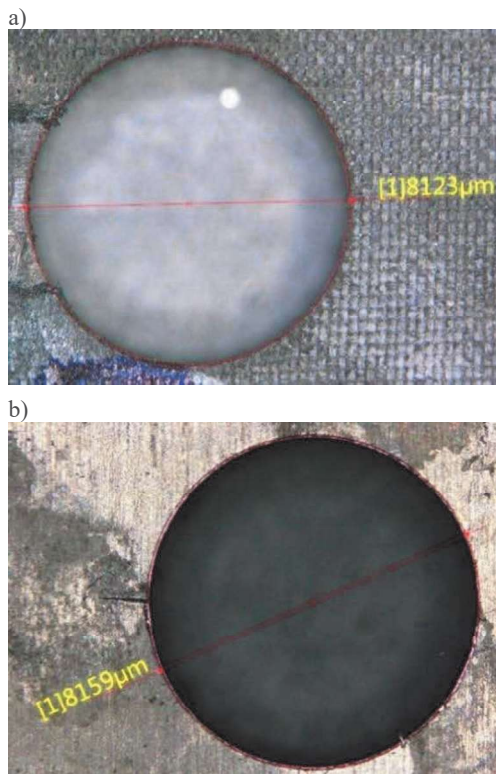


**Fig. 11.** Hole after drilling with drill bit diameter  $\emptyset 8$  for CFRP/Al drilling strategy and cutting speed  $v_c = 30$  m/min: a) at the entry of the drill bit, b) at the exit of the drill bit

The quality of post-drilling holes in layered materials was also assessed visually to identify material defects after machining. Special attention was paid to

holes drilled in the CFRP composite. Figures 11–13 show images of the holes for selected cutting conditions.

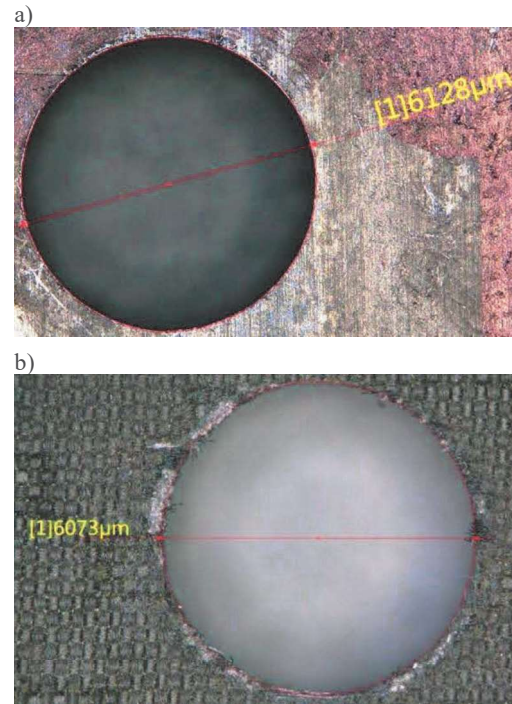


**Fig. 12.** Hole after drilling with drill bit diameter  $\emptyset 6$  for Al/CFRP drilling strategy and cutting speed  $v_c = 60$  m/min: a) at the entry of the drill bit, b) at the exit of the drill bit

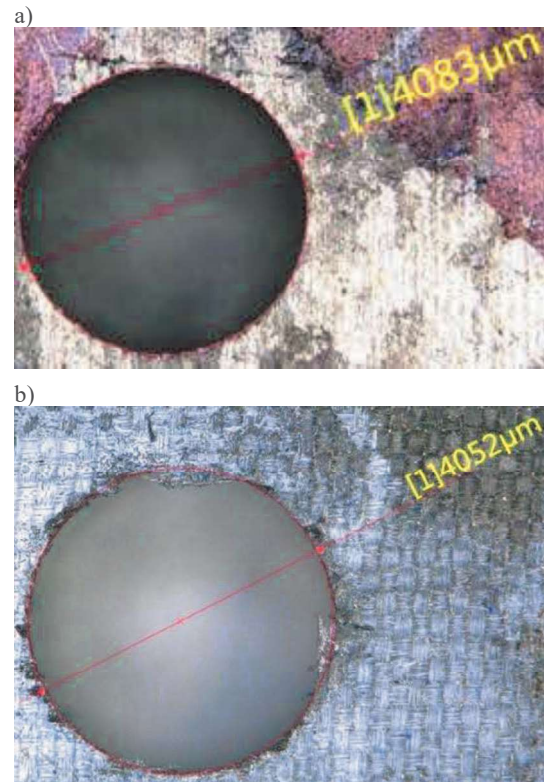


**Fig. 13.** Hole after drilling with drill bit diameter  $\emptyset 4$  for Al/CFRP drilling strategy and cutting speed  $v_c = 30$  m/min: a) at the entry of the drill bit, b) at the exit of the drill bit

A visual evaluation of the holes after machining made it possible to note the occurrence of typical forms of destruction of polymer composites. During machining of the aluminum alloy there was mainly breaking of the hole, as a result of which in most cases holes with larger diameters were obtained in the metal layer than in the composite layer. Making holes in the CFRP composite was associated with the occurrence of typical forms of damage in fiber composites, i.e. torn and undercut fibers, matrix cracking, delamination and inclusions of aluminum chips. The occurrence of these defects led in many cases to a reduction in the diameter of the machined holes, resulting in lower value of the hole accuracy index D and misleadingly indicating holes with higher dimensional accuracy. This phenomenon can directly lead to difficulties in the implementation of the assembly process.

#### 4. Conclusions

The aim of this study was to determine the effect of the cutting conditions on the quality of holes drilled in a layer structure. Based on the results obtained, it was found that the lowest value of the hole accuracy index D (0.010) indicating the best hole accuracy, was obtained at the exit of the cutting tool when using the drill bits with diameters  $\varnothing 8$  mm and  $\varnothing 4$  mm and the cutting speed  $v_c = 90$  m/min and the Al/CFRP drilling strategy. The highest value of the D index (0.059) was observed at the exit of the drill bit diameter  $\varnothing 6$  mm using the cutting speed of  $v_c = 30$  m/min and the Al/CFRP drilling strategy.

Both at entry and exit of cutting tools, the D index was most influenced by the drill bit diameter, while the interaction of the three considered independent variables ( $v_c \times \varnothing \times S$ ) had no statistically significant effect on its values.

The CFRP/Al drilling strategy proved to be a better machining method compared to the Al/CFRP drilling strategy due to the avoidance of delamination of the composite material at the exit of the cutting tool.

Increasing the cutting speed for most of the cases considered resulted in an increase in the dimensional accuracy of holes made in the composite layer and its deterioration in the metal layer.

The dimensional accuracy of holes made in metal-polymer composite layered materials should not be analyzed solely by means of the index D. A visual assessment taking into account post-machining defects on the machined surfaces should also be considered.

#### References

Alagan, N.T., Sajja, N.T., Gustafsson, A., Savio, E., Ghiotti, A., Bruschi, S., & Bertolini, R. (2023). Investigation of the

quality of Al-CFRP stacks when drilled using innovative approaches. *CIRP Journal of Manufacturing Science and Technology*, 43, 260–272. doi.org/10.1016/j.cirpj.2023.04.011.

Changze Sun, Ch., Albastani, H., Phadnis, V.A., Saleh, M.N., Cantwell, W.J., & Guan, Z. (2023). Improving the structural integrity of foam-core sandwich composites using continuous carbon fiber stitching. *Composite Structures*, 324, 117509. doi.org/10.1016/j.compstruct.2023.117509.

Cieciela, K. (2022). Study on the Machinability of Glass, Carbon and Aramid Fiber Reinforced Plastics in Drilling and Secondary Drilling Operations. *Advances in Science and Technology Research Journal*, 16(2), 57–66. doi.org/10.12913/22998624/146079.

Doluk, E. (2023). Comparison of hole quality after drilling and helical milling of the Al/CFRP stacks. *Technologia I Automatykacja Montażu (Assembly Techniques and Technologies)*, 122(4), 3–12. doi.org/10.7862/tiam.2023.4.1.

Ergün, E., Uzun, G., & Altaş, S. (2021). Evaluation of the effects of drilling parameters, tool geometry and core material thickness on thrust force and delamination in the drilling of sandwich composites. *Surface Review and Letters*, 28(12), 2150112. doi.org/10.1142/S0218625X21501122.

Hosseinkhani, H., Zhang, X., Liu, Q., & Nasiruddin, M. (2024). Enhancing impact energy absorption in composite sandwich structures through synergistic smart material integration. *Results in Engineering*, 21(3), 101902. doi.org/10.1016/j.rineng.2024.101902.

Isbilir O., & Ghassemieh, E. (2013). Numerical investigation of the effects of drill geometry on drilling induced delamination of carbon fiber reinforced composites. *Composite Structures*, 105, 126–133. doi.org/10.1016/j.compstruct.2013.04.026.

Kausar, A., Ishaq A., Rakha, S.A., Eisa, M.H., & Diallo, A. (2023). State-Of-The-Art of Sandwich Composite Structures: Manufacturing-to-High Performance Applications. *Journal of Composites Science*, 7(3), 102. doi.org/10.3390/jcs7030102.

Kilickap, E. (2020). Optimization of cutting parameters on delamination based on Taguchi method during drilling of GFRP composite. *Expert Systems with Applications*, 37(8), 6116–6122. doi.org/10.1016/j.eswa.2010.02.023.

Melentiev, R., Priarone, P.C., Robiglio, M., & Settineri, L. (2016). Effects of Tool Geometry and Process Parameters on Delamination in CFRP Drilling: An Overview. *Procedia CIRP*, 45, 31–34. doi.org/10.1016/j.procir.2016.02.255.

Natarajan, E., Markandan, K., Sekar, S.M., Varadaraju, K., Nesappan, S., Albert Selvaraj, A.D., Lim, W.H., & Franz, G. (2022). Drilling-Induced Damages in Hybrid Carbon and Glass Fiber-Reinforced Composite Laminates and Optimized Drilling Parameters. *Journal of Composites Science*, 6(10), 310. doi.org/10.3390/jcs610031.

Saoudi, J., Zitoun, R., Gururaja, S., Salem, M., & Mezleni, S. (2018). Analytical and experimental investigation of the delamination during drilling of composite structures with core drill made of diamond grits: X-ray tomography analysis. *Journal of Composite Materials*, 52(10), 1281–1294. doi:10.1177/0021998317724591.

- Yang, B, Wang, H., Chen, Y., Fu, K., & Li, Y. (2021). Experimental evaluation and modelling of drilling responses in CFRP/honeycomb composite sandwich panels. *Thin-Walled Structures*, 169, 108279. doi.org/10.1016/j.tws.2021.108279.
- Zhang, Z., Myler, P.; Zhou, E., & Zhou, R. (2020). Strength and Deformation Characteristics of Carbon Fibre Reinforced Composite Wrapped Aluminium Foam Beams. *Journal of Composites Science* 6(10), 288. doi.org/10.3390/jcs6100288.

## DESIGN FOR ASSEMBLY: WRIST ORTHOSIS DESIGN CONCEPTS PROPOSALS

### PROJEKTOWANIE POD KĄTEM MONTAŹU: PROPOZYCJE KONCEPCJI ORTEZ NADGARSTKA

Abigail MACHAJ<sup>1,\*</sup>, Kinga SOBCZYK<sup>2</sup>, Wiktoria WOJNAROWSKA<sup>1</sup> ,  
Michał WANIC<sup>1</sup> 

<sup>1</sup> Department of Physics and Medical Engineering, Faculty of Mathematics and Applied Physics, Rzeszow University of Technology, al. Powstańców Warszawy 6, Rzeszow, Poland

<sup>2</sup> Department of Culture and Media, Faculty of Humanities, SWPS University, Chodakowska 19/31, Warsaw, Poland

\* Corresponding author: 173095@stud.prz.edu.pl

#### Abstract

This study investigates the integration of modern engineering techniques, including 3D scanning and additive manufacturing, in the design and production of wrist orthoses. The research aims to enhance orthotic devices by proposing three innovative fastening methods - Velcro straps, screws, and magnets - designed for use with 3D-printed orthoses. The study outlines the entire process from patient hand scanning to the final orthosis creation, emphasizing the precision and customization afforded by these advanced technologies. The proposed designs are intended to improve the comfort, effectiveness, and usability of orthoses for patients with musculoskeletal dysfunctions. The findings demonstrate the potential for significant advancements in personalized medical devices, offering new avenues for rehabilitation and patient care.

**Keywords:** orthosis, 3D scanning, additive manufacturing, fastening methods

#### Streszczenie

Niniejsze badanie analizuje integrację nowoczesnych technik inżynierskich, w tym skanowania 3D i wytwarzania przyrostowego, w projektowaniu i produkcji ortez nadgarstka. Celem badań jest udoskonalenie urządzeń ortotycznych poprzez zaproponowanie trzech innowacyjnych metod mocowania – pasków na rzep, śrub oraz magnesów – przeznaczonych do użytku z ortezami wydrukowanymi w technologii 3D. Badanie przedstawia cały proces, od skanowania dłoni pacjenta po końcowe stworzenie ortozy, z naciskiem na precyzję i możliwość personalizacji, jakie zapewniają te zaawansowane technologie. Proponowane projekty mają na celu poprawę komfortu, skuteczności i użyteczności ortez dla pacjentów z dysfunkcjami układu mięśniowo-szkieletowego. Wyniki wskazują na potencjał znacznych postępów w dziedzinie spersonalizowanych urządzeń medycznych, oferując nowe możliwości w zakresie rehabilitacji i opieki nad pacjentem.

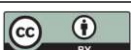
**Słowa kluczowe:** orteza, skanowanie 3D, wytwarzanie przyrostowe, metody mocowania

## 1. Introduction

Modern medicine requires innovative solutions to meet the growing expectations of patients in developed and emerging regions. The ongoing improvement of existing treatment methods is driven by advances not only in medicine but also in technology and engineering. Rapid prototyping (RP), particularly additive

manufacturing (AM), has become popular in recent years as an alternative method for making prototypes. For example, in the automotive industry, AM prototypes are used to validate engineering processes (Jiménez et al. 2019).

AM techniques, due to their speed and cost-effectiveness, have attracted interest in various fields, including industrial design, automotive, manufactur-



ing, as well as medicine, and biomedical and tissue engineering. In the medical field, 3D printing is used to create custom medical products such as prostheses, implants, surgical tools, and orthoses that are tailored to the anatomy of the patient (Jiménez et al. 2019; Kumar and Sarangi, 2021; Pathak et al. 2023).

Implants, prostheses, and orthoses are designed to correct and alleviate dysfunction and disability (Hailey, 1995). However there are some differences between them. An implant is an internal medical device placed in the body to replace or support a damaged structure, a prosthesis is a device that replaces a missing body part, and an orthosis is an external medical device used to stabilize, support, or correct musculoskeletal dysfunctions (Chen et al. 2016).

Using AM techniques for the production of medical devices allows them to be precisely tailored to each patient's unique anatomical characteristics, increasing comfort and effectiveness. Achieving these features is unlikely with universally mass-produced medical devices. Furthermore, this type of personalization leads to better patient outcomes and greater satisfaction (Pathak et al. 2023; Tserovski et al. 2019). Furthermore, as indicated by Boretti (2024), 3D printing reduces production time and costs while offering patients the same or better functionality. This is particularly beneficial in cases where traditional methods can cause discomfort due to bulkiness or poor fit (Oud et al. 2021).

Musculoskeletal disorders (MSDs) are prevalent conditions that significantly affect the quality of life and functional abilities of individuals. As indicated by Mohaddis (2023), the use of orthoses as a treatment modality for these disorders is common and well documented in clinical practice. Orthoses, commonly used to limit joint mobility, have been employed for more than 150 years in the treatment of various musculoskeletal conditions (Mohaddis, 2023). However, they are not only useful for immobilizing fractured limbs; postoperative (Donato et al. 2023), and rehabilitative (Mohaddis, 2023) variants are also popular. They are routinely prescribed to improve mobility in children and adults with neurological disorders such as cerebral palsy, Charcot-Marie-Tooth disease, stroke, and multiple sclerosis (Haque et al. 2023); there is also potential to help with Patellofemoral pain syndrome (PFPS) (Smith et al. 2015).

Orthotic devices (orthoses) can be divided into three types based on the anatomical structure of the human body: spinal orthoses, upper limb orthoses, and lower limb orthoses. Names indicate the specific anatomical joints and body parts that each orthosis supports (Nouri et al. 2023). For example, one of the orthoses for the upper extremity is a wrist hand

orthosis (WHO) that covers the wrist and hand, including fingers (Costa, 2024). A rehabilitative WHO, such as a dynamic splint, is used to aid in recovery of hand function after injury, surgery, or neurological condition (Gilanlioğulları and Soyer, 2024; Zhou et al. 2024). This type of orthosis provides controlled movement and support to the fingers, wrist, and hand, facilitating the rehabilitation process by improving range of motion, reducing stiffness, and assisting in muscle re-education (Yang et al. 2021).

Different types of fastening are used in the design of orthoses. For instance, Poier et al. (2021b) used for their design of wrist orthosis velcro straps, Li and Tanaka (2018) used elements such as velcro straps and screws, whereas Paterson (2013) used a very unique fastening system that incorporates rubber bands. Moreover, the parts of orthosis could be also connected by a snap fit shape connection, such as in the project by Górski et al. (2020).

The choice of fastening plays a critical role in both the effectiveness and user comfort of the orthosis. According to the study by Ferrari et al. (2021), fastening systems significantly influence how well an orthosis fits the user. A popular option for fastening rehabilitative orthoses due to their ease of adjustment and user-friendly application are velcro straps, as confirmed by studies such as Poier et al. (2021b), Li and Tanaka (2018), and Cazon et al. (2017). 3D-printed orthoses offer significant advantages over traditional methods such as mass-produced ones or plaster casts (Oud et al. 2021; Zhou et al. 2024). These include superior customization, allowing precise tailoring to an individual's unique anatomical features, which enhances both comfort and effectiveness (Oud et al. 2021). Using AM to produce custom orthoses allows for rapid and cost-effective production (Pathak et al. 2023). Moreover, it allows for a more flexible approach to design (Zhou et al. 2024). The freedom of design enables the creation of highly specialized and personalized orthoses, including the incorporation of various fastening methods to meet the needs and preferences of the individual patient (Li and Tanaka, 2018; Jiménez et al. 2019).

The goal of this paper is to design a personalized 3D-printed wrist orthosis, while also exploring different fastening methods to enhance its adherence and effectiveness. To achieve this, a systematic product development process was followed, including concept generation, evaluation of various fastening options (such as Velcro straps, screws, and magnets), and final product specification. This paper will discuss the design process, the selection criteria for fastening methods, and the overall performance of the personalized orthosis.

## 2. Materials and Methods

### 2.1. Product Development

At the beginning of product development was to conduct a literature review to generate ideas for different fastening methods for wrist orthoses. Based on the literature, many options for fastening mechanisms were identified. The authors chose two of them: Velcro straps due to their popularity and screws, which were used in only one project. Screws were also considered due to their availability and low cost. Moreover, it was decided to use for fastening mechanism elements such as magnets. To the best of the authors' knowledge, the use of such elements for fastening mechanisms of wrist orthoses has not been described in the literature, and the authors believe it is worth considering due to the availability and low cost of magnets. The next step of product development was to design an initial model of orthosis.

### 2.2. 3D Model Creation and Processing Workflow

To obtain models of wrist orthoses, modern digital technologies such as 3D scanners and computer-aided design (CAD) were chosen, similar to the approach of Zhou et al. (2024). The creation of the orthosis can be divided into several key stages as shown on Fig. 1.

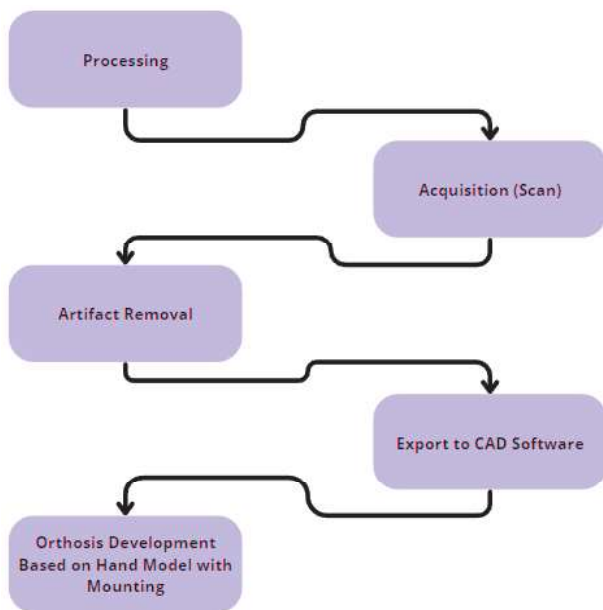


Fig. 1. Process for model creation

Initially, detailed requirements for the orthosis and scanning parameters are established. The patient's hand is then scanned with a 3D scanner to create an accurate digital anatomical model. Preliminary data processing follows to remove any unwanted artifacts and noise, which is crucial for maintaining the model's accuracy. The cleaned model is then exported to specialized CAD software for further processing and

customization of the orthosis design. Finally, the orthosis is designed based on the hand model, incorporating appropriate fastenings such as Velcro straps, screws, or magnets, and is thoroughly analyzed for ergonomics, user comfort, and functionality.

#### 2.2.1. Initial model of wrist orthosis

The development of the orthosis began with establishing detailed requirements and scanning parameters. The patient's hand was then scanned using an advanced 3D scanner, creating a digital anatomical model that captured even the smallest details (Kumar and Sarangi 2021; Silva et al. 2024). In this project, a detailed scan of the left hand was performed using the Shining 3D EinStar scanner. This device is equipped with three infrared VCSEL structured light projectors, which are safe for the eyes. The scanning process began with preparing the subject's hand, which included positioning the hand correctly and ensuring optimal lighting conditions to achieve the best results. The entire scanning procedure took less than thirty minutes, demonstrating the efficiency and advanced technology of the device.

Upon completing the scan, an initial 3D model of the hand was obtained, as shown in Fig. 2A. Unfortunately, this model contained several artifacts, which could have resulted from various factors such as hand movement during scanning or light reflections. Preliminary data processing using tools available in the dedicated scanning software (EXStar Software) removed those artifacts and noise to ensure the model accurately reflected the patient's anatomy. This involved using filtering algorithms that automatically identified and eliminated unwanted elements.

The next step was model segmentation, which involved isolating the selected area from the rest of the scanned object. This was achieved by cutting the model with a suitably positioned cutting plane (Fig. 2B). This step was crucial to obtain a model encompassing only the part of the arm and hand where the orthosis would be applied (Fig. 2C). Isolating just this section of the scanned model reduced the file size, which in turn made further processing of the model require less computational power.

The obtained model contained various irregularities, including gaps in the scanned surface. Therefore, it underwent further corrections. The repair of the model was carried out using the same software by employing available editing tools. One of these tools allowed for the reconstruction of missing parts of the model.

As a result of the implemented corrections, a digital model of the upper limb was obtained. The 3D model of the hand was not only free from disturbances but also accurately reflected the real

proportions and anatomical structures. This model served as a reference during the modeling of the final orthosis, ensuring the orthosis would meet the requirement of being customized.

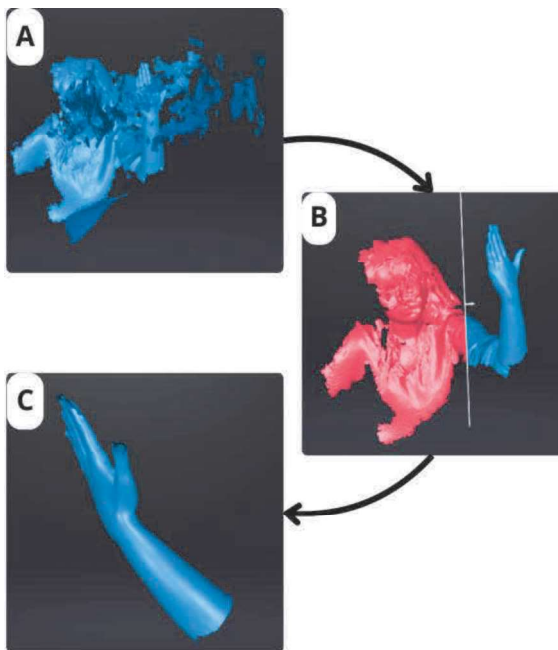


**Fig. 2.** Three stages of processing the 3D model of the left hand: (A) Raw scan with artifacts, (B) Segmentation and extraction of the hand, (C) Final, corrected 3D model of the hand

The cleaned model was exported to CAD software for further processing and customization. However, the import required file format conversion, as the initial model was a point cloud. This conversion was performed in SpaceClaim software by approximating spline curves. The process involved covering the point cloud with elementary NURBS (non-uniform rational B-spline) surface patches. The resulting model was saved in STEP format.

After importing the model into Autodesk Inventor, the first step was to divide it along the axis of the hand using planes. The model was divided into several parts, where hand outlines were created. Then, the loft function was used, allowing these outlines to be selected and a figure to be formed based on them. This resulted in a model of the hand based on the previous scan, which could be further refined (Fig. 3).

The next step was to create an offset, which involved forming a new solid offset 5 mm from the hand. Another offset was created on this offset model, also offset by 5 mm, which formed the orthosis skeleton. After performing these operations, the hand model and the first offset could be turned off, allowing direct work on the orthosis skeleton.

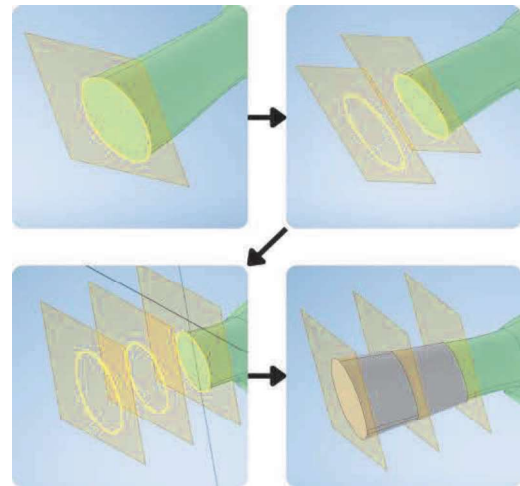


**Fig. 3.** Shows the stages of creating the model in Autodesk Inventor. The process starts with setting up reference planes (top-left) that define the cross-sectional profiles of the object. More planes are added (top-right) to capture different sections along the length of the model. These cross-sections (bottom-left) guide the creation of the final 3D shape (bottom-right), resulting in a solid model ready for further processing

Cutouts for the fingers and a cutout at the back of the hand, which allows easy insertion of the hand into the orthosis, were added to the orthosis skeleton. The next step was to round all parts to eliminate potential sources of discomfort. As a result, a 3D model of the wrist orthosis without the fastening mechanism was obtained. The next step was to incorporate suitable fastenings, such as Velcro straps, screws, or magnets.

### 2.2.2. First design - Velcro Fastenings

The first and simplest concept implemented was the use of Velcro fastenings. This straightforward, yet innovative idea offers an exceptional ease of application and removal, particularly important for individuals with rheumatological conditions or those who need to wear an orthosis intermittently. Velcro fastenings provide several advantages, including simplicity and adjustability. They are incredibly user-friendly, allowing quick and effortless fastening and unfastening of the orthosis, greatly facilitating daily use (Bader and Percy 1982). Additionally, the adjustability of Velcro enables a customized fit to the individual's specific needs, enhancing comfort and minimizing any discomfort associated with wearing the orthosis, which is crucial for individuals with limited mobility.

#### Implementation:

1. **Cutout Creation:** Initially, a suitable cutout is made at the back of the orthosis (see photo Fig. 4.) to create the required space for mounting the Velcro.
2. **Velcro Attachment:** The next step involves attaching the Velcro in the designated area,

which required sewing it onto the orthosis. This step required precision and skill to ensure that the Velcro was securely attached and would perform effectively in regular use.



Fig. 4. Back (left photo) and front (right photo) of the 3D model for velcro fastenings

### 2.2.3. Second design - Screws

The second concept involved the use of screws. In this approach, the orthosis is divided into two parts and printed separately. Special protruding areas were added to allow the orthosis to be screwed together. This method is particularly suitable for individuals who use an orthosis as a substitute for a cast and do not remove it by themselves. The use of screws makes the orthosis more secure and robust, ensuring that it remains in place and functions effectively without the risk of being accidentally removed.

#### Implementation:

1. **Design Modification:** The orthosis is divided into two parts and printed separately, with special protruding areas to enable it to be screwed together.
2. **Square Nut Integration:** Cutouts are added inside the back half of the orthosis to accommodate a square nut (Fig. 5.) This square nut, printed along with the orthosis, provides a more stable and stronger base for the screws.



Fig. 5. Front (left photo) and close-up of the place for square nut (right photo) of the 3D model for screws

### 2.2.4. Third design - Magnets

The third concept involves dividing the orthosis into two parts, similar to the previous designs, but using neodymium magnets to join them. This approach is particularly suitable for people who need a secure and easy-to-use fastening method without the complexity of screws or the manual effort required for Velcro. Neodymium magnets provide a strong and reliable connection, ensuring that the orthosis remains firmly in place while also being easy to detach when necessary. This option is ideal for people who require frequent adjustments or need to remove the orthosis quickly and effortlessly, such as children, the elderly, or people undergoing physical therapy.

#### Implementation:

1. **Design and Integration:** The orthosis is divided into two parts, with neodymium magnets embedded within the material to join them (Fig. 6.).
2. **Magnet Placement:** Internal placement of the magnets ensures that the orthosis remains lightweight and maintains its aesthetic appearance.

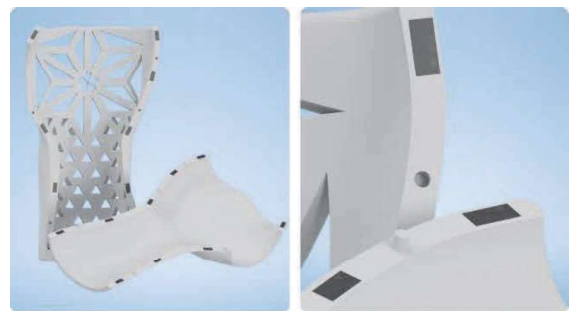


Fig. 6. Two elements of the orthosis (left photo) and close-up of the place for magnets (right photo) of the 3D model for magnets

### 2.5. Material Selection for 3D printing

For FDM printing, materials such as PLA, ABS, PA (nylon), PETG, TPU, HIPS, and PVA can be used, offering diverse physical and chemical properties. For printing an orthosis mostly three materials are used ABS, PA, and PLA (Jaworska and Podsiadło 2019; Kumar and Sarangi 2021; Steck et al. 2023).

ABS (Acrylonitrile Butadiene Styrene) is characterized by high strength, rigidity, and durability. It is resistant to heat and chemicals, making it suitable for applications requiring high mechanical resistance. Its printability is also high, allowing for precise models. However, ABS is less environmentally friendly compared to PLA and requires a higher printing temperature, which can affect energy costs (Poier et al. 2021a).

PA (Polyamide, Nylon) is distinguished by exceptional strength and durability, as well as resistance to

chemicals and heat. It is flexible and abrasion-resistant, making it ideal for applications requiring high resistance to mechanical stress (Kumar and Sarangi 2021). However, printing with nylon can be more demanding due to its hygroscopic nature, which means that it absorbs moisture from the environment.

PLA (Polylactic Acid) is a biodegradable and easy-to-print material, making it environmentally friendly and suitable for less experienced users. PLA offers moderate strength and rigidity, which are sufficient for many medical applications, such as orthoses (Poier et al. 2021b). Its heat and chemicals resistance is lower than ABS and nylon, but its ecological potential and ease of processing make it an ideal choice for this project [9].

## 2.6. Printing of the chosen design

The first design, which incorporated a fastening mechanism using Velcro straps, was chosen for 3D printing. As shown in Fig. 7B, the model was imported into PrusaSlicer 2.7.4.

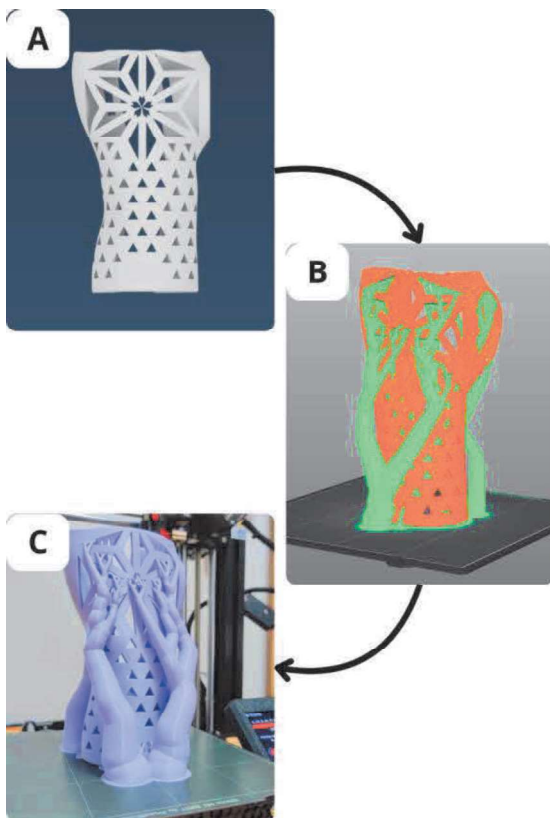


**Fig. 7.** Stages of the printing process. A - model in Autodesk Inventor. B - model imported into a dedicated Prusa slicer program to prepare it for 3D printing. C - printed model on Prusa Mini 3D printer

The model was positioned on the build plate without internal infill, as its geometric design provides sufficient structural support. Supports were added for

overhanging sections to ensure an accurate reproduction of complex geometries. The printing settings included a layer height of 0.2 mm, a nozzle temperature of 210°C, and a bed temperature of 60°C. PLA was the material used for the print. Fig. 7C shows the model after printing on the Prusa Mini, still attached to the build plate with supports intact. The total print time was approximately 5.5 hours, with a material consumption of 90 grams.

After printing is completed, the model is removed from the printer and the supports are removed. Organic supports used in this process allow for easy and quick removal. A special open-cell foam was adhered to the inside of the orthosis.

This particular type of foam was chosen for its properties that allow for better skin breathability, reducing hand sweating, and minimizing the risk of skin irritation. However, several alternatives can also be considered depending on the specific needs of the user.

An alternative to open-cell foam is the use of silicone gel. It is often used because of its ability to evenly distribute pressure, which is beneficial for users with more sensitive skin. Silicone gel also provides excellent cushioning and is very durable, making it an ideal choice for orthoses requiring long-term use.

In the pre-planned locations, fastening elements were placed to ensure proper fit and stability of the orthosis on the patient's limb. In this case, Velcro straps were sewn in which can be seen in Fig. 8. This fastening method allows the user to easily and quickly adjust the orthosis to their individual needs and ensures that the orthosis stays in place.



**Fig. 8.** Front and back view of the finished wrist orthosis

## 3. Results and Discussion

The primary objective of this study was to create personalized 3D printed wrist orthosis. The secondary goal was to prepare concepts of three distinct fastening methods for 3D printing orthosis with: Velcro, screws and neodymium magnets. This process started with precise 3D scanning of the patient's hand. The scanned data were then utilized to create accurate digital anatomical models using advanced CAD software,

allowing for the customized design of the orthoses. Each orthosis design incorporated one of the three fastening methods.

Velcro fastenings significantly enhance user-friendliness, especially for those who need to use such medical equipment regularly. Moreover, those are among the most popular methods (especially commercial wise) (Aranceta-Garza and Ross 2021; Coppard and Lohman 2020). This method is so common due to its cost-effectiveness. Velcro straps are inexpensive and readily available, making them an economical choice for orthosis fastenings. Furthermore, the ease of replacement ensures that the orthosis can maintain its functionality over a long period, even if the Velcro wears out. However, one of the challenges associated with Velcro is its tendency to lose grip over time, especially with frequent use and exposure to dirt and moisture (Bader and Pearcy 1982). This requires regular inspection and maintenance to ensure that the orthosis remains effective. Additionally, visible fastening elements can sometimes affect the aesthetic appeal of the orthosis, which may be a consideration for some users.

Using screws for fastening could offer superior stability and durability. Screws are believed to provide a tight and secure connection, ensuring that the orthosis remains in place and does not shift or become loose during use. This is particularly important for patients who require a high level of support and immobilization (Haje and de Podestá Haje 2009). However, the use of screws also presents some challenges. The assembly and disassembly of screws require tools, which can be time-consuming and complex for some users. This can be a disadvantage for patients who need to adjust or remove their orthosis frequently. Additionally, protruding screw heads can sometimes cause discomfort or irritation, especially if they are not adequately cushioned or covered.

Using neodymium magnets to fasten the orthosis could offer several significant advantages. One of the primary benefits is the elimination of external visual changes to the orthosis, as the magnets are embedded within the material and do not alter its appearance, maintaining a discreet and aesthetically pleasing look. Additionally, the internal placement of the magnets would ensure that the orthosis remains lightweight and comfortable to wear. Neodymium magnets also could provide a unique advantage in terms of ease of use. They require minimal effort to fasten and unfasten, making them an excellent choice for individuals with limited hand strength or dexterity. This can significantly enhance the user experience, particularly for elderly patients or those with conditions affecting their motor skills. However, there are some drawbacks to using neodymium magnets. These magnets are brittle

and can easily crack or become damaged if handled carelessly. They are also prone to corrosion in humid conditions, which can affect their longevity and performance. Additionally, neodymium magnets are more expensive to produce than other fastening methods, which can increase the overall cost of the orthosis (Kapustka et al. 2020). The overall summary of the three concepts is presented in Table 1.

**Table 1.** Specification of the designs

	First design	Second design	Third design
Fastening type	Velcro	Screws and nuts	Neodymium magnets
Orthosis	Single part	Two parts	Two parts
Fastening mounting	Sewing	Nut inside orthosis	Magnets inside orthosis
Appearance	Velcro straps under orthosis	Screw visible on both sides	No visual indication
Suggested usage	Universal	Fractures	For kids
Bonding strength	Medium	High	Low
Degree of difficulty	Medium	Hard	Easy

#### 4. Conclusions

This study presents valuable insights into the practical application of various fastening methods for wrist orthoses, providing preliminary guidance for their development. This may prove helpful to engineers involved in the development of orthoses.

This study represents a novel application of neodymium magnets for fastening wrist orthoses, to the best of the authors' knowledge. Although magnets are easy to use, they appear brittle, prone to corrosion, and expensive. Further development is needed to enhance their suitability for orthotic applications. Magnets may be suitable for low-load or supplementary uses, possibly in combination with other fastening methods.

Velcro straps emerged as a user-friendly and cost-effective fastening option. It is recommended for wrist and hand orthoses due to its ease of use and adaptability. However, Velcro may wear out over time and has some aesthetic drawbacks that should be considered in design.

Screws as a fastening mechanism offer stability and durability but require tools for adjustment and may cause discomfort. They are best suited for applications where high stability is essential.

Overall, while Velcro is currently the most practical and popular choice, ongoing innovation in fastening technologies is crucial for advancing orthotic solutions. The research highlights the importance of continuing to explore and develop new fastening

methods to enhance the functionality and user experience of orthoses.

#### 4.1. Future research directions

The study underscores the need for further research to explore advances in magnetic fastenings and hybrid methods. Long-term user studies are also recommended to refine these fastening technologies and improve orthosis design, ensuring greater effectiveness and user comfort.

#### References

- Aranceta-Garza, A., & Ross, K. (2021). A comparative study of efficacy and functionality of ten commercially available wrist-hand orthoses in healthy females: Wrist range of motion and grip strength analysis. *Frontiers in Rehabilitation Sciences*, 2. <https://doi.org/10.3389/freco.2021.687554>.
- Bader, D. L., & Percy, M. J. (1982). *Material properties of Velcro fastenings*. *Prosthetics & Orthotics International*, 6(2), 93–96. <https://doi.org/10.3109/03093648209166773>.
- Boretti, A. (2024). A perspective on 3D printing in the medical field. *Annals of 3D Printed Medicine*, 13(100138), 100138. <https://doi.org/10.1016/j.stlm.2023.100138>.
- Cazon, A., Kelly, S., Paterson, A. M., Bibb, R. J., & Campbell, R. I. (2017). Analysis and comparison of wrist splint designs using the finite element method: Multi-material three-dimensional printing compared to typical existing practice with thermoplastics. *Proceedings of the Institution of Mechanical Engineers. Part H, Journal of Engineering in Medicine*, 231(9), 881–897. <https://doi.org/10.1177/0954411917718221>.
- Costa, R. (2024). Terminology and classification of orthoses for upper limbs. *Journal of Hand Therapy: Official Journal of the American Society of Hand Therapists*, 37(3), 489–491. <https://doi.org/10.1016/j.jht.2023.08.011>.
- Chen, R. K., Jin, Y., Wensman, J., & Shih, A. (2016). Additive manufacturing of custom orthoses and prostheses—A review. *Additive Manufacturing*, 12, 77–89. <https://doi.org/10.1016/j.addma.2016.04.002>.
- Coppard, B. M., & Lohman, H. (2020). *Introduction to orthotics: A clinical reasoning & problem-solving approach*. Elsevier/Mosby.
- Donato, Z., Gonzalez, D., Markowitz, M., & Gjolaj, J. (2024). Postoperative spinal orthoses: Types and outcomes. *The Journal of the American Academy of Orthopaedic Surgeons*, 32(5), 211–219. <https://doi.org/10.5435/JAAOS-D-23-00498>.
- Ferrari, A. L. M., Medola, F. O., & Sandnes, F. E. (2021). How do orthoses impact ease of donning, handwriting, typewriting, and transmission of manual torque? A study of three prefabricated wrist-hand orthoses. *Journal of Prosthetics and Orthotics: JPO*, 33(3), 168–174. <https://doi.org/10.1097/jpo.0000000000000344>.
- Gilanloğulları, N., & Soyer, K. (2024). Effects of dynamic wrist-hand splints for patients with rheumatoid arthritis: A systematic review. *Prosthetics and Orthotics International*. doi:10.1097/PXR.0000000000000355.
- Górski, F., Wichniarek, R., Kuczko, W., Żukowska, M., Lulkiewicz, M., & Zawadzki, P. (2020). Experimental studies on 3D printing of automatically designed customized wrist-hand orthoses. *Materials*, 13(18), 4091. <https://doi.org/10.3390/ma13184091>
- Hailey, D. M. (1995). Orthoses and prostheses. *International Journal of Technology Assessment in Health Care*, 11(2), 214–234. <https://doi.org/10.1017/s026646230000684x>
- Haje, S. A., & de Podestá Haje, D. (2009). Orthopedic approach to pectus deformities: 32 years of studies. *Revista Brasileira de Ortopedia (English Edition)*, 44(3), 191–198. [https://doi.org/10.1016/s2255-4971\(15\)30067-7](https://doi.org/10.1016/s2255-4971(15)30067-7)
- Haque, A., Parsons, H., Parsons, N., Costa, M., Redmond, A., Mason, J., ... & Kearney, R. (2023). Use of cast immobilization versus removable brace in adults with an ankle fracture: two-year follow-up of a multicentre randomized controlled trial. *The Bone & Joint Journal*, vol. 105-B no. 4, str. 382–388. <https://doi.org/10.1302/0301-620x.105b4.bjj-2022-0602.r3>.
- Jaworska, N., & Podsiadło, H. (2019). Technologia druku 3D jako szansa dla środowiska naturalnego. *Acta Poligraphica*, vol. 14.
- Jiménez, M., Romero, L., Domínguez, I. A., Espinosa, M. del M., & Domínguez, M. (2019). Additive manufacturing technologies: An overview about 3D printing methods and future prospects. *Complexity*, 2019(1), 1–30. <https://doi.org/10.1155/2019/9656938>.
- Kapustka, K., Ziegmann, G., Klimecka-Tatar, D., & Nakonczy, S. (2020). Process management and technological challenges in the aspect of Permanent magnets recycling - the second life of neodymium magnets. *Manufacturing Technology*, 20(5), 617–624. <https://doi.org/10.21062/mft.2020.098>.
- Kumar, R., & Sarangi, S. K. (2021). 3D-Printed Orthosis: A Review on Design Process and Material Selection for Fused Deposition Modeling Process. *Advances in Materials Processing and Manufacturing Applications: Proceedings of iCADMA 2020*, 531–538.
- Li, J., & Tanaka, H. (2018). Rapid customization system for 3D-printed splint using programmable modeling technique – a practical approach. *3D Printing in Medicine*, 4(1). <https://doi.org/10.1186/s41205-018-0027-6>.
- Mohaddis, M. (2023). Enhancing functional rehabilitation through orthotic interventions for foot and ankle conditions: a narrative review. *Cureus*. <https://doi.org/10.7759/cureus.49103>.
- Nouri, A., Wang, L., Li, Y., & Wen, C. (2023). Materials and manufacturing for ankle-foot orthoses: A review. *Advanced Engineering Materials*, 25(20). <https://doi.org/10.1002/adem.202300238>.
- Oud, T. A., Lazzari, E., Gijsbers, H. J., Gobbo, M., Nollet, F., & Brehm, M. A. (2021). Effectiveness of 3D-printed orthoses for traumatic and chronic hand conditions: A scoping review. *PLOS ONE*, 16(11). <https://doi.org/10.1371/journal.pone.0260271>.
- Paterson, A. M. J. (2013) Digitisation of the splinting process: exploration and evaluation of a Computer Aided Design approach to support Additive Manufacture, [PhD thesis, Loughborough University, Loughborough]. University Repository: [https://repository.lboro.ac.uk/articles/thesis/Digitisation\\_of\\_the\\_splinting\\_process\\_exploration\\_and\\_evaluation\\_of\\_a\\_computer\\_aided\\_design\\_approach\\_to\\_support\\_additive\\_manufacture/9350207?file=26674988](https://repository.lboro.ac.uk/articles/thesis/Digitisation_of_the_splinting_process_exploration_and_evaluation_of_a_computer_aided_design_approach_to_support_additive_manufacture/9350207?file=26674988).

- Pathak, K., Saikia, R., Das, A., Das, D., Islam, M. A., Pramanik, P., Parasar, A., Borthakur, P. P., Sarmah, P., Saikia, M., & Borthakur, B. (2023). 3D printing in Biomedicine: Advancing Personalized Care through additive manufacturing. *Exploration of Medicine*, 1135–1167. <https://doi.org/10.37349/emed.2023.00200>.
- Poier, P. H., Arce, R. P., Rosenmann, G. C., Carvalho, M. G., Ulbricht, L., & Foggiatto, J. A. (2021). Development of modular wrist, hand and finger orthosis by additive manufacturing. *Research, Society and Development*, 10(15). <https://doi.org/10.33448/rsd-v10i15.22707>.
- Poier, P. H., Weigert, M. C., Rosenmann, G. C., de Carvalho, M. G., Ulbricht, L., & Foggiatto, J. A. (2021). The development of low-cost wrist, hand, and finger orthosis for children with cerebral palsy using additive manufacturing. *Research on Biomedical Engineering*, 37(3), 445–453. <https://doi.org/10.1007/s42600-021-00157-0>.
- Silva, R., Silva, B., Fernandes, C., Morouço, P., Alves, N., & Veloso, A. (2024). A Review on 3D Scanners Studies for Producing Customized Orthoses. *Sensors*, 24(5), 1373.
- Smith, T. O., Drew, B. T., Meek, T. H., & Clark, A. B. (2015). Knee orthoses for treating patellofemoral pain syndrome. *Cochrane Database of Systematic Reviews*, 2015(12). <https://doi.org/10.1002/14651858.cd010513.pub2>.
- Steck, P., Scherb, D., Witzgall, C., Miehl, J., & Wartzack, S. (2023). Design and additive manufacturing of a passive ankle-foot orthosis incorporating material characterization for fiber-reinforced PETG-CF15. *Materials*, 16(9), 3503. <https://doi.org/10.3390/ma16093503>.
- Tserovski, S., Georgieva, S., Simeonov, R., Bigdeli, A., Röttinger, H., & Kinov, P. (2019). Advantages and disadvantages of 3D printing for pre-operative planning of Revision Hip Surgery. *Journal of Surgical Case Reports*, 2019(7). <https://doi.org/10.1093/jscr/rjz214>.
- Yang, Y.-S., Tseng, C.-H., Fang, W.-C., Han, I.-W., & Huang, S.-C. (2021). Effectiveness of a new 3D-printed dynamic hand-wrist splint on hand motor function and spasticity in chronic stroke patients. *Journal of Clinical Medicine*, 10(19), 4549. doi:10.3390/jcm10194549.
- Zhou, M., Sun, C., Naghavi, S. A., Wang, L., Tamaddon, M., Wang, J., & Liu, C. (2024). The design and manufacturing of a Patient-Specific wrist splint for rehabilitation of rheumatoid arthritis. *Materials & Design*, 238(112704), 112704. doi:10.1016/j.matdes.2024.112704.

## JET ENGINE – CONSTRUCTION AND MODERN DEVELOPMENT EXAMPLES

### TURBINOWY SILNIK ODRZUTOWY – BUDOWA I PRZYKŁADY OBECNEGO ROZWOJU

Arkadiusz GARWOL<sup>1</sup> 

<sup>1</sup> Gdańsk University of Technology, ul. Gabriela Narutowicza 11/12, 80-233 Gdańsk, Poland

\* Corresponding author: s201995@student.pg.edu.pl, tel.: (+48) 535 950 026

#### Abstract

The article presents the construction and operating principle of a turbine jet engine. The basic types of engines of this type are presented, such as single-rotor single-flow jet engines, single-flow dual-rotor engines (which are another development version of single-rotor engines), as well as dual-flow engines which are currently most commonly used in passenger aviation, and contra-rotating propeller engines and turbine propeller engines. Also presented their applications, such as propulsion of various types of. In the further part of this paper, the development trends of turbine jet engines are described, based on patents that have been granted in recent years. One of the cited patents is the use of a fuel cell to power an electric motor used to start a turbine jet engine. Also presented the concept of an electric motor providing propulsion of aircraft. An engine of this type is devoid of a turbine and a combustion chamber, and the machine shaft rotates only using electricity. The purpose of this paper is to present the construction and operating principles of turbine jet engines and examples of the current development of this type of construction, as well as to determine future development trends for those devices.

**Keywords:** engine, power unit, drive, airplane, aircraft

#### Streszczenie

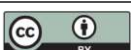
W artykule przedstawiono budowę oraz zasadę działania turbinowego silnika odrzutowego. Przedstawiono podstawowe rodzaje silników tego typu, jakimi są odrzutowe silniki jednowirnikowe jednoprzepływowe, jednoprzepływowe silniki dwuwirnikowe (które są kolejną wersją rozwojową silników jednowirnikowych), a także silniki dwuprzepływowe która są obecnie najczęściej stosowane w lotnictwie pasażerskim oraz silniki przeciwbieżne śmigłowentylatorowe i turbinowe silniki śmigłowe. Przedstawiono również ich zastosowania jakimi jest napęd różnych typów statków powietrznych. W dalszej części niniejszego artykułu, przedstawiono tendencje rozwojowe turbinowych silników odrzutowych, na podstawie patentów jakie zostały przyznane w ciągu ostatnich lat. Jednym z przywołanych patentów jest zastosowanie ogniwa paliwowego do zasilania silnika elektrycznego, użytego do rozruchu turbinowego silnika odrzutowego. Przedstawiono również koncepcję elektrycznego silnika zapewniającego napęd statków powietrznych. Silnik tego typu, jest pozbawiony turbiny i komory spalania, a wał maszyny obraca się jedynie za pomocą energii elektrycznej. Celem niniejszego artykułu jest przedstawienie budowy oraz zasady działania turbinowych silników odrzutowych i przykładów obecnego rozwoju tego typu konstrukcji oraz określenie przyszłych tendencji rozwojowych tych urządzeń.

**Słowa kluczowe:** silnik, zespół napędowy, napęd, samolot, statek powietrzny

## 1. Introduction

The jet engine is the basic element of every aircraft. It is responsible for providing the necessary thrust to generate lift, which allows the aircraft to fly.

The design of jet engines has clearly evolved along with the development of the entire aviation industry. This was a consequence of the continuous process of improving air transport, in the face of the growing demand for the provision of air services - in the form



of transporting people and goods. It should also be clearly emphasized that there would be no development of civil aviation without the development of military aviation. For a very long time, modern solutions were first introduced in military applications, and when they proved themselves there, they were transferred to the civilian environment.

A jet engine consists of several sections, which are: inlet, compressor, combustion chamber, turbine and nozzle. An optional addition is an afterburner, which allows both achieving high forward flight speed and minimizing the time to reach this speed. A cross-sectional diagram of a jet engine is shown on Fig. 1.

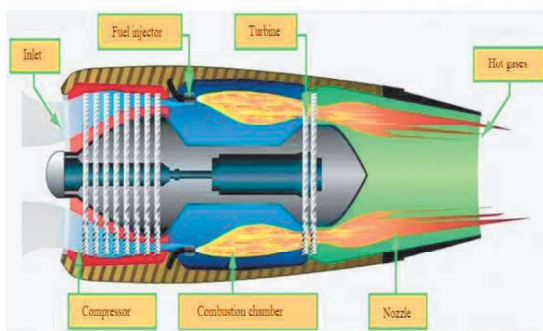


**Fig. 1.** Cross- sectional diagram of a jet engine,  
(Source Aeronautics-Guide)

The principle of operation of a turbine jet engine is based on the increase in pressure of the air flowing into the device, with the help of the related pressure it flows into the combustion chamber, where it is mixed with fuel using evaporators or swirlers. It is in the combustion chamber that the resulting fuel-air mixture ignites, which generates thrust. Next, the air with an increased temperature falls onto the turbine blades. The main task of the turbine is to drive the compressor. It is worth noting that this component is the most critical part of the entire engine. This is because the turbine operates at a very high temperature, in the range of several hundred to a thousand °C. Due to the enormous thermal loads and those caused by continuous rotation, it is considered that the turbine determines the parameters of the entire jet engine.

The engine is started in several different ways. For this purpose, it is possible to use the APU Auxiliary Power Unit. This device is placed at the rear of the aircraft, the purpose of which is to provide electrical energy to a miniature electric engine, coupled to the jet engine. The value of this speed is several thousand rpm. By giving the shaft rotational speed, the rotational speed of other engine components also increases. Through this action, it is possible to supply fuel to the chamber and ignite it, which causes a further increase in rotational speed.

As mentioned, the design of the jet engine has evolved as a result of the growing requirements placed on aircraft structures. Therefore, the purpose of this article is to present the various variants of turbine jet engines, the history of their development, and the effects of current research.

## 2. Types of turbine jet engines

Due to the specificity of their operation, turbine jet engines have several basic variants. This division results directly from the different conditions of use of such devices, and consequently different values of rotational speed achieved by aircraft power units. In addition, it is necessary to distinguish the application of a given type of engine. An engine used in civil aviation will look different than in military aviation. This results from the specificity of this use. For example, before a civil aircraft takes off, it is necessary to start the engine earlier in order for the power unit to gain temperature and for the materials to adapt to the working conditions. In military aircraft, we deal with different situations. Often, when we deal with the so-called duty pair (a pair of aircraft standing on the airport tarmac in combat readiness), the pilots of these machines must immediately start the aircraft to perform the flight task after receiving the order. As a result, they do not warm up the engine. Therefore, engines used in military machines are exposed to greater thermal loads and those resulting from the action of axial and radial forces of the operating engine.

### 2.1. Single-rotor single-flow jet engine

These are the simplest turbine engines. Currently, they are used as a drive for "target aircraft" or flying models and some types of cruise missiles or unmanned reconnaissance aircraft. They can also be used as a source of power for selected types of disposable, training, training-combat aircraft (Stefan Szczeciński and others).

The advantages of this type of construction are the simplicity of the design, which enables low-cost production and operation. The value of available thrust, generated by single-rotor, single-flow turbine jet engines, oscillates within the range of 1,000 daN to 2,000 daN for combat aircraft and within the range of several to a dozen or so daN for flying models. Fluctuations in the generated thrust value in such a wide range result from the very versatile use of this type of engine. The disadvantages of these single-flow machines are the limitation of operational parameters due to their simplicity of construction. These limited parameters are the short engine start-up time, or the acceleration and deceleration time.

These, the simplest jet engines are not economical. The value of the specific fuel consumption is slightly lower than 1 kg/daNh, during operation in the cruise range. As the described design developed technically, air vents, adjustable guide vanes (in the case of axial compressors), adjustable outlet nozzles or adjustable guide vanes were introduced. The improvement of the device allowed for a significant reduction of the acceleration and deceleration time without the risk of stalling and damage to turbine or compressor parts. As a result of these changes, the safety of flying and the efficiency of performing aviation tasks improved (Stefan Szczeciński and others). A cross-section diagram of this type of engine is shown in Fig. 2.

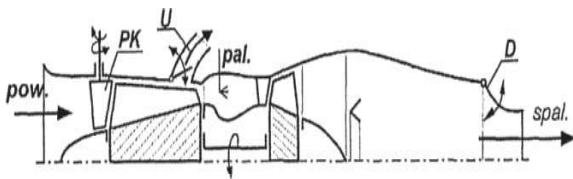


Fig. 2. "Diagram of a jet engine with a mechanized pre-flow channel: PK – adjustable compressor guide vanes, U – air release after the compressor, D – adjustable outlet nozzle, pal. – fuel, pow. – air, spal. – exhaust gases (Stefan Szczeciński and others)"

An example of an aircraft equipped with a single-flow turbine jet engine is the MiG-19 aircraft, which were used in Poland at the turn of the 1950s and 1960s. They were equipped with a pair of RD-9B engines developed in the design office of Alexander Mikulin. In engines of this type, air bleed was used during start-up and operation in the lower range of rotational speeds with simultaneous, full opening of the exhaust nozzle flaps (as is the case during afterburner operation). During engine operation in the cruise range, the flaps were partially closed. In turn, full deflection was used at the maximum range of rotational speeds during flight without afterburner (Stefan Szczeciński and others).

One of the modifications of the single-flow engine was the introduction of a twin-rotor design.

## 2.2. Single-flow dual-rotor jet engine

The diagram of a single-flow, dual-rotor engine is shown in Fig. 3.

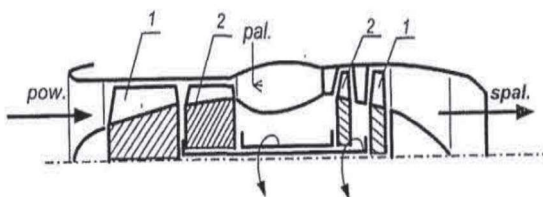


Fig. 3. Single-flow, twin-rotor jet engine: 1 – low-pressure rotor, 2 – high-pressure rotor, 3 – medium-pressure rotor, 4 – afterburner, pal. – fuel, spal. – exhaust gas, (Source: Stefan Szczeciński and others)

An example of a used twin-flow turbine jet engine is the British Olympus engine from Bristol Aero Engines. It was introduced into production in 1955, and its development versions (Rolls-Royce/SNECMA Olympus 593) were used to power the famous supersonic Concorde aircraft. Twin-rotor engines were used in Poland, and their production began in 1959. An example of an engine from this period is the R11F-300 engine, equipped with an afterburner. It was the powerplant of various versions of the Mig-21 aircraft. A characteristic feature of the R11F-300 engine is its compact design, and the eight-stage compressor (4+4) it is equipped with allows for obtaining a compression ratio of about 8.6...9.55. The value of the obtained compression ratio depends on the engine version (Stefan Szczeciński and others).

## 2.3. Dual-flow engine

Dual-flow engines are now commonly used in civil passenger aviation. An example design of this type of engine is shown in Fig. 4.

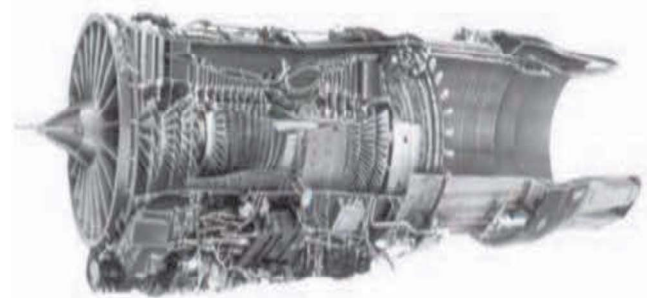


Fig. 4. A dual-flow turbine jet engine equipped with a mixer and afterburner F100- PW-229, (Source: Paweł Przybyłek, Andrzej Komorek)

As we can see in the above diagram and from the name of the presented device, it is equipped with a second air flow, bypassing the basic engine components. Thanks to this, the dual-flow engine allows to achieve cruising speeds in the range of 0.8...0.85 Ma with a simultaneous, moderate fuel consumption of 0.35...0.3 kg/daNh (Stefan Szczeciński and others).

## 2.4. Contra-rotating propeller engine

The next step in the development of turbine jet engines was the introduction of the contra-rotating propeller fan drive.

The term "counter-rotation" means the swirling of the air behind the propeller, which increases the amount of air flow energy moving parallel to the direction of flight, which is converted into thrust of the power unit. The diagram of the described counter-rotating propeller-fan engine is shown in Fig. 5.

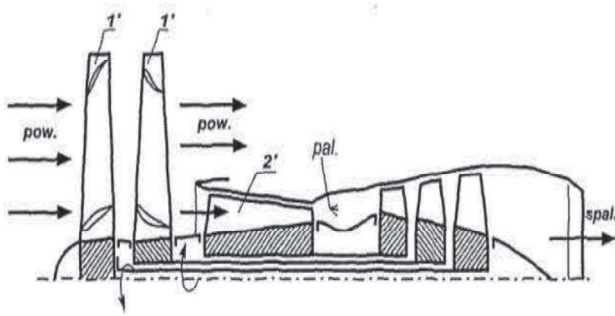


Fig.5. “Diagram of a propeller-fan engine: 1’ – propeller-fan, 2’ – exhaust gas generator compressor, pal. – fuel, pow. – air, spal. – exhaust gases”, (Source Stefan Szczeciński and others)

One example of the use of aircraft powertrains equipped with a fan-type engine is the An-70 aircraft.

### 2.5. Turbine propeller engine

Turbine propeller engines are characterized by the addition of a propeller to a turbine jet engine in order to improve the operating properties of the power unit in a limited speed range. An example of the use of this type of engine is passenger and transport aircraft that do not require high-speed flight and are characterized by low acquisition and use costs. These include, for example, the ATR-72 civil aircraft or the CASA C-295 military transport aircraft. The diagram of the turbine propeller engine is shown in Fig. 6.

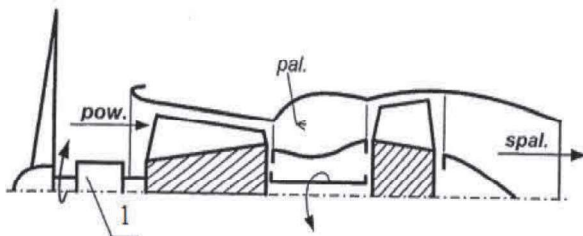


Fig. 6. Schematic diagram of a single-rotor propeller engine: 1 – rotor of the exhaust gas generator, pal – fuel, spal. – exhaust gas, pow – air, (Source Stefan Szczeciński and others)

Currently, turbine propeller engines are implemented as single- or, currently more often, twin-rotor, which can be considered as another development version of this type of drive.

### 3. Current development of turbine jet engines

Nowadays, more and more attention is paid to renewable energy sources. This has its resonance in the face of quite clear efforts to reduce greenhouse gas emissions. These voices of opposition to CO2 emissions do not bypass the aviation industry either. In 2016, in the United States, a patent was filed for an aircraft engine using a fuel cell.

### 3.1. Application of fuel cell in turbine jet engine

A fuel cell is used to obtain electrical energy from hydrogen fuel.

The need to develop an engine using a fuel cell arose from the imperfections of the compressor. If the compressor reaches the so-called threshold temperature, the air can interfere with the operation of the compressor, which causes difficulties with lubrication of this element. As a consequence, the amount of work necessary to compress the air to a given pressure increases. Consequently, this can adversely affect the efficiency of the compressor, i.e. not using its full potential. The solution to this shortcoming may be the elimination of air heat energy from the compressor section, which is provided by the engine using a fuel cell. In addition, the use of a fuel cell provides power to the electric motor used to start the turbine jet engine, and the final product of the chemical reaction in the fuel cell is water (General Electric Company, Mohammed El Hacin Sennoun). The diagram of this solution is shown in Fig. 7.

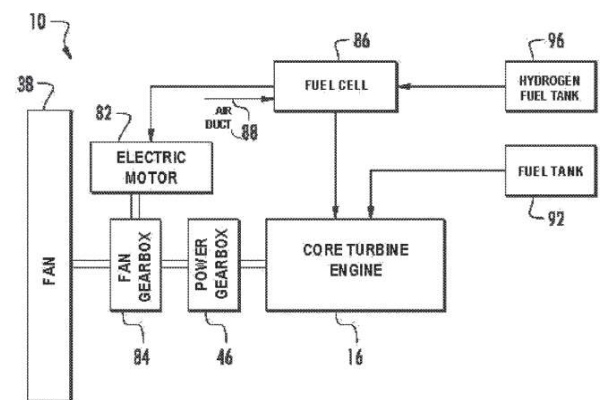


Fig. 7. Schematic representation of a turbine jet engine equipped with a fuel cell: 10 – axial direction, 16 – sample core of a turbine jet engine, 38 – variable pitch fan, 46 – power transmission, 82 – electric motor, 84 – fan transmission, 86 – fuel cell, 96 – hydrogen tank as fuel for the fuel cell, (Source: General Electric Company, Mohammed El Hacin Sennoun)

### 3.2. The concept of a fully electric turbine jet engine

Another interesting concept is a motor that uses electric current to rotate the motor shaft. A diagram of such a concept is shown in Fig. 8.

As we can see in the diagram above, this engine lacks a combustion chamber and a turbine. This is due to the lack of need to burn fuel in this type of engine, because the entire engine is, in a way, one large electric coil.

Due to the lack of most moving parts in the engine and the absence of a combustion process, this type of engine is characterized by overall greater operational

safety (Codrin-Gruie Cantemir), which is of great importance in the aviation industry.

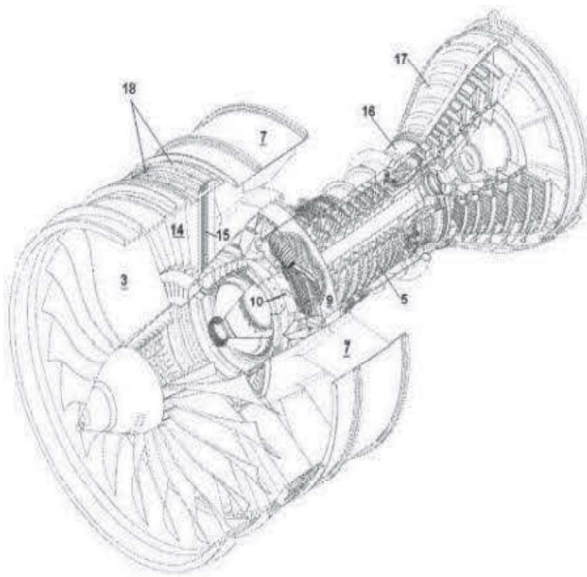


**Fig. 8.** Isometric diagram of a hybrid turbine jet engine: 3 – main rotor, 5 – high-pressure compressor, 7 – mid box, 9 – rotor, 10 – bent spokes, 14 – booster, 15 – cooling channels, 16 – combustion section, 17 – turbine assembly sockets, (Source: Codrin-Gruie Cantemir)

#### 4. Development of fuel technology in aviation

Currently, there is an increasing talk about the need to reduce emissions of harmful greenhouse gases. This also applies to aviation. One of the alternative solutions is the use of biofuels in aviation. Currently, one of the most interesting works on a fuel competitive to the currently used E85 and AGE 85 is the work on synthetic fuel from biomass. They are conducted by Prof. Jan Rusek from Purdue University's School of Astronautics and Aeronautics Engineering, founder of Swift Enterprises Ltd. A characteristic feature of this type of fuel is the lack of oxygen compounds. Its composition is 82.5% m/m mesitylene and 16.9% m/m isopentane and trace amounts of other hydrocarbons. After completing the initial tests, Swift, in cooperation with the FAA, conducted engine tests. The test results confirmed low wear of engine parts, no contamination and good fuel quality. The only drawback was a slight deformation of the fuel pump diaphragm. It should be mentioned, however, that tests of the discussed fuel type were carried out on piston engine (Zbigniew Pagowski).

When considering substitutes for fuels currently used in turbine jet engines, it is worth mentioning the concept of Bio-Jet fuel. This is a fuel produced using oil processed from biomass. The first breakthrough event related to the use of this type of fuel was obtaining certification for Jet fuel produced from microalgae by the American company Solazyme.

Using this type of fuel, the reduction of greenhouse gas emissions reaches 95%. Work on Bio-Jet fuels was also carried out by Boeing, which in 2008, in cooperation with UOP LLC Honeywell, presented the practical application of Bio-Jet fuel, developed by itself a year earlier under a government contract. This type of fuel also meets the requirements for fuels used in turbine jet engines, i.e. a freezing point value of less than  $-47^{\circ}\text{C}$  and a flash point exceeding  $38^{\circ}\text{C}$ . The fuel developed by UOP was called Bio-SPK. Moreover, in the case of this fuel, the basis for production was a process involving catalytic hydrorefining of oil from microalgae and vegetable oils.

In favor of the use of biofuels, there are a number of other important factors. By using a significant degree of raw material conversion, we can minimize the amount of waste products. In addition, through greater production of biofuels, it is possible to obtain the use for current agricultural wastelands or poor quality soils (Bohdan Naumienko, Grzegorz Rarata). This will be a huge advantage for supporting domestic agriculture. It should also be taken into account that in the production of more technologically advanced fuels, it is necessary to use algae or microalgae, which entails the need to build appropriate infrastructure and have the appropriate experience.

#### 5. Conclusions and summary

The turbine jet engine is an extremely innovative device. Despite the various concepts presented in this study, this device is still being developed. This is due to the constantly increasing demand for innovative devices of this type, as aviation has more and more applications. This has been demonstrated by the current war in Ukraine, where various types of aircraft are very often used - including drones.

Given the ongoing international tensions, we can expect an increase in interest in the design of turbine jet engines, which will be designed to provide propulsion for aircraft in such a way that they can gain air superiority in confrontation with enemy machines. Based on history, we can say that technology used for military needs will pass into the civilian environment and gain its new applications there.

In civil aviation, more and more attention is being paid to the need to protect the environment. It is often said that the conventional aircraft propulsion, which is constituted by turbine jet engines, should be replaced by renewable energy sources. The solution to this problem may be the use of the engine presented in this study, in which a fuel cell is used to drive an electric starter engine, or the presented hybrid turbine jet engine, in which electricity plays the leading role. It is also worth emphasizing that this type of energy can be

generated using renewable sources, but it can also be easily transferred and stored, for example using batteries. In the coming years, we can expect the development of just such a source of aircraft propulsion.

The development of fuel technology is inevitable if we are to talk about the development of the aviation industry. This is related to the current efforts to reduce greenhouse gases. The use and further development of biofuels in aviation will have a huge impact on the shape of the aviation industry in the coming years.

This study can be an introduction to a more in-depth analysis of the development of turbine jet engines, which is extremely innovative and has enormous research potential. It can also be a review of the individual types of turbine jet engines currently in use.

## References

- Aeronautics-Guide *Aircraft Gas Turbine Engines Types and Construction* <https://www.aircraftsystemstech.com/p/gas-turbine-engines-types-and.html>.
- Cantemir C. G. *Fully integrated hybrid electric jet engine* <https://patentimages.storage.googleapis.com/f3/11/98/6fb7ea18926ec6/US10308365.pdf> United States Patent.
- Naumienko B., Rarata G. *Aktualne potrzeby i możliwości wytwarzania paliwa typu Bio-Jet*, Prace Instytutu Lotnictwa. <https://yadda.icm.edu.pl/baztech/element/bwmeta1.element/baztech-article-BSW4-0094-0010>
- Sennoun M. El. H., General Electric Company, *Hybrid Propulsion system for a gas turbine engine including engine including a fuel cell*, United States Patent <https://patentimages.storage.googleapis.com/c0/6c/c1/280fe302497539/US10774741.pdf>.
- Szczeciński S., Balicki W., Chachurski R., Głowacki P., Kawalec K., Kozakiewicz A., Szczeciński J. *Lotnicze zespoły napędowe*, Wojskowa Akademia Techniczna.
- Pągowski Z. *Badania i eksploatacja samolotów zasilanych biopaliwami* Prace Instytutu Lotnictwa. <https://bibliotekanauki.pl/articles/213820>.
- Przybyłek P., Komorek A. *Modularyzacja w budowie lotniczych wojskowych statków powietrznych* [https://web.archive.org/web/20180422132148id\\_/http://www.tiam.pl/Archiwum/pdf/2009\\_04s19.pdf](https://web.archive.org/web/20180422132148id_/http://www.tiam.pl/Archiwum/pdf/2009_04s19.pdf).

## MODULAR TECHNOLOGICAL LINE FOR ASSEMBLING AND TESTING CAR DAMPERS

### MODUŁOWA LINIA TECHNOLOGICZNA DO MONTAŻU I TESTOWANIA AMORTYZATORÓW SAMOCHODOWYCH

Robert TOMASIEWICZ<sup>1</sup>

<sup>1</sup> CEO, ELPLC S.A., Rozwojowa 28, Tarnów, Poland

\* Corresponding author: [robert.tomasiewicz@elplc.com](mailto:robert.tomasiewicz@elplc.com)

#### Abstract

Suspension systems are integral for a safe and comfortable driving experience, with dampers as crucial components. The global car dampers market is expected to grow due to the increasing demand regardless of the type of cars drive technologies. Manufacturers are focused on innovating both damper design and production processes, aiming for better energy and material efficiency. Product analysis, line layout, and quality control are essential components of the damper assembly and testing process, ensuring that finished components are of high quality and meet market demands. Proper dampers assembly line design is essential for efficient mass production, requiring meticulous planning of products, processes, and line layout. Methodologies like concurrent engineering aid in addressing design challenges efficiently, fostering innovations and collaboration among designers, engineers, and decision-makers. The purpose of project described in this study was to develop an modular assembly line for dampers integrating innovative features for efficiency, including high measurement accuracy in functional testing, automation, and cycle time reduction, meeting the diverse needs of OEMs and Tier1 companies worldwide. This project received funding form Smart Growth Operational Program 2014-2020 under designation POIR.01.01.

01-00-1029/17-00. The line has been developed, tested and implemented and this study focuses on the description of the individual line modules.

**Keywords:** dampers, dampers assembly lines, concurrent engineering, assembly line designing

#### Streszczenie

Układy zawieszenia są warunkiem bezpiecznej i komfortowej jazdy, a amortyzatory są ich kluczowymi elementami. Oczekuje się, że globalny rynek amortyzatorów samochodowych będzie rósł ze względu na rosnący popyt niezależnie od rodzaju technologii napędowych samochodów. Producenci koncentrują się na innowacjach zarówno w projektowaniu amortyzatorów, jak i procesów produkcyjnych, dążąc do większej efektywności energetycznej i materiałowej. Analiza produktu, układ linii i kontrola jakości są niezbędnymi elementami procesu montażu i testowania amortyzatorów, zapewniając, że gotowe produkty mają wysoką jakość i spełniają wymagania rynku. Prawidłowy projekt linii montażowej amortyzatorów jest warunkiem wydajnej produkcji masowej, wymagającej skrupulatnego planowania produktów, procesów i układu linii. Metodologie, takie jak concurrent engineering, pomagają w efektywnym rozwiązywaniu problemów projektowych, wspierając innowacje i współpracę między projektantami, inżynierami i decydentami. Celem projektu opisanego w tym badaniu było opracowanie modułowej linii montażowej amortyzatorów integrującej innowacyjne funkcje w celu zwiększenia wydajności, w tym wysoką dokładność pomiaru w testach funkcjonalnych, automatyzację i skrócenie czasu cyklu, spełniającej zróżnicowane potrzeby producentów OEM i firm Tier1 na całym świecie. Projekt ten uzyskał dofinansowanie w ramach Programu Operacyjnego Inteligentny Rozwój 2014-2020 pod oznaczeniem POIR.01.01.01-00-1029/17-00. Linia została opracowana, przetestowana i wdrożona, a niniejsze opracowanie koncentruje się na opisie poszczególnych modułów linii.

**Słowa kluczowe:** amortyzatory samochodowe, linie montażu amortyzatorów, concurrent engineering, projektowanie linii montażowej



### 1. Introduction

Suspension systems play a key role in ensuring a safe, smooth and comfortable ride. Their essential components are damping elements, which are typically telescopic hydraulic dampers. The use of dampers in cars is crucial for active safety or collision prevention. They enable maintaining the appropriate tire-to-ground grip on various types of surfaces and stabilizing the vehicle during driving and braking (Gardulski, 2009). It is therefore not surprising that with the growing demand for passenger cars and light commercial vehicles in emerging economies and the growing trend of electric and hybrid vehicles, the global automotive damper market is expected to grow at a CAGR of 5.4% over the next ten years (2023-2033) (Persistence Market Research, 2023). Manufacturers at the OEM (car manufacturers) and Tier1 (component suppliers) level are therefore looking not only for innovations in the design of dampers themselves but also in the modernization of their production. This applies particularly to the optimization of energy and material consumption and quality testing with appropriate precision.

#### 1.1. Dampers types

Modern car suspensions are complex mechanical systems with damping and elastic elements. Dampers found in vehicle suspensions can be divided into two groups with several varieties: mono-tube and twin-tube (Fig. 1). Main differences between those groups was collected in Table 1.

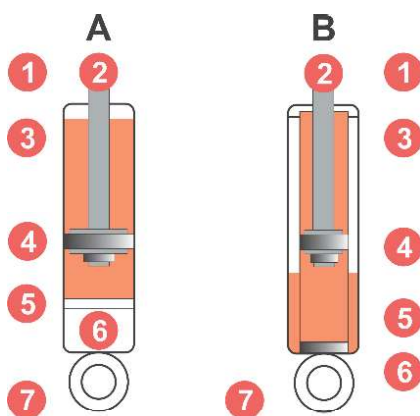


**Fig. 1.** Simplified drawing of the mono-tube (A) and twin-tube (B) variants. A(1) – external tube; A(2) – piston rod; A(3) – oil chamber; A(4) – piston valve; A(5) – floating piston; A(6) – gas chamber; A(7) – mounting element; B(1) – external tube; B(2) – piston rod; B(3) – pressure tube; B(4) – piston valve; B(5) – gas chamber; B(6) – base valve; B(7) – mounting element

**Twin-tube basic** – consists of two cylinders placed one on top of the other: an internal pressure cylinder and an external reserve cylinder. There is a compression valve in the lower part.

**Twin-tube gas** – its general structure is very similar to the simple version. Nitrogen is introduced into the external cylinder at low pressure. This has resulted in a reduction of the foaming or aeration of the oil. The foaming phenomenon occurring when the temperature of the twin-tube system increases causes hydraulic fluid leakage. Dampers of this type predominate in modern vehicle suspensions.

**PSD – position sensitive damper** – another evolution of the twin-tube damper in the gas version. The pressure cylinder is additionally equipped with grooves here, improving the freedom of movement of the piston in the middle range of the stroke, in the so-called comfort zone. On the other hand, the piston moves with significantly less freedom when driving on very irregular surfaces, resulting in a “stiffening” of the suspension and greater control over the vehicle – the so-called control zone.

**ASD – acceleration sensitive damper** – change in the design of the compression valve enabling a faster response to individual unevenness.

**Table 1.** Mono-tube and twin-tube comparison

Mono-tube	Twin-tube
<b>Main differences</b>	
<ul style="list-style-type: none"> <li>• The housing is also a cylinder with a piston rod guidance system, oil and gas placed inside</li> <li>• A floating piston separates the oil and gas chambers</li> <li>• High gas pressure</li> </ul>	<ul style="list-style-type: none"> <li>• Pressure pipe, cylinder is placed inside the outer pipe (housing). The piston rod moves inside the pressure pipe.</li> <li>• Oil and gas chambers are not separated</li> <li>• Low gas pressure</li> </ul>
<b>Pros</b>	
<ul style="list-style-type: none"> <li>• Stable damping force over time due to larger oil capacity and better heat dissipation</li> <li>• Larger piston valve allows for greater precision while generating low damping forces</li> <li>• No restrictions on the mounting angle</li> <li>• Easier heat dissipation</li> <li>• No oil aeration due to the separation of the chambers</li> </ul>	<ul style="list-style-type: none"> <li>• It is easier to ensure sufficient lift with a shorter structure length</li> <li>• The use of a base valve allows the use of low gas pressure – driving is more comfortable</li> <li>• Low gas pressure avoids seal stress and reduces friction</li> <li>• The damper remains functional with minor damage to the outer tube</li> </ul>
<b>Cons</b>	
<ul style="list-style-type: none"> <li>• Construction more susceptible to damage (single tube, which is also a housing)</li> <li>• Maintaining sufficient stroke is made more difficult by the serial arrangement of the chambers, the greater length of the damper for the same stroke</li> <li>• High gas pressure causes a "stiffer ride", greater seal stress and friction</li> </ul>	<ul style="list-style-type: none"> <li>• Lower oil capacity</li> <li>• Smaller piston rod</li> <li>• The design limits the possible mounting angles</li> <li>• The oil and gas chambers are not separated, which causes aeration and foaming as the temperature increases</li> </ul>

**Mono-tube** – initially patented in the 1950s by Bilstein (Shelton, Chris, 2017). consists of a single pressure cylinder containing both gas and oil medium. It has two pistons: a working piston and a floating piston, which move inside the pressure tube. Both pistons completely separate the liquid and gas components of the damper. This type of damper has a longer design than the twin-tube, and has no directionality of assembly. The nitrogen pressure is 1,8÷2,5 MPa.

The output force of the damper is described by a complex function of the hydraulic valve characteristics, dimensions, oil properties, gas pressure and fluid phenomena, e.g. cavitation. Numerous works (Lang, 1977; Duym, Steins, Reybrouck, 1997; Farjoud, Ahmadian, Craft, Burke, 2012; Ferdek, Łuczko, 2012; Czop, Sawik, 2011) describe methods of modeling the output damping force and provide specific models, such as the dynamic model of the Lang twin-tube damper (Lang, 1977). These models are of key importance for the functional characteristic test stations of dampers (Sikora, 2017).

## 1.2. Assembly lines design process basics

Assembly lines (ALs) represent a fundamental method in mass production environments, facilitating efficient product assembly through the use of workers, dedicated machines, or robots. The design of assembly lines is crucial as it directly impacts the efficiency and productivity of manufacturing processes. The primary objective of assembly systems is to enhance line efficiency by maximizing the throughput-to-cost ratio, which is essential for maintaining competitiveness in today's demanding markets (Adham et al., 2013; Nourmohammadi, Eskandari, 2017).

Assembly line design (ALD) involves several critical components, including the development of products, processes, and plant layout, which must be meticulously planned before the actual construction of the assembly line. This planning phase is vital as it ensures that the assembly line operates smoothly and efficiently once implemented. The interaction of these components throughout various stages of the ALD process is crucial for achieving optimal performance (Bortolini et al., 2017; Triki et al., 2017). For instance, the assembly line balancing problem (ALBP) is a well-known challenge that arises during the design phase, where the goal is to allocate tasks among workstations in a manner that minimizes idle time and maximizes productivity (Nourmohammadi, Eskandari, 2017; Cohen, 2013).

Product analysis includes a review of the product design, adhering to standard 'design for assembly' (DFA) principles and task precedence constraints. The

module focused on operating modes and techniques suggests suitable assembly methods, as well as possible modes for each task: manual, automated or robotic (Gao et al., 2019).

The line layout (LL) problem is divided into logical and physical layouts. Developing the logical layout involves distributing tasks among the stations along the assembly line, whereas the physical layout determines the placement of stations, resources, conveyors, buffers, and other equipment on the factory floor. The logical LL includes challenges such as assembly line balancing (ALB) and resource planning (RP). In manual assembly lines, balancing aims to equalize the workload across stations. For hybrid assembly lines (HALs), where operations can be performed manually or with robots and automated machinery, resource planning assigns resources to tasks and allocates tasks to stations (Yamada et al., 2022).

Companies implemented various practices and tools, collectively known as concurrent engineering (CE), to enhance their product development processes. CE is fundamentally characterized by the integration of diverse expertise to address design challenges effectively and efficiently. The essence of CE lies in assembling the right individuals at the right time to collaboratively identify and resolve design problems. This approach fosters a multidisciplinary environment where various stakeholders, including system engineers, designers, and decision-makers, can engage in real-time discussions and problem-solving activities. As noted by, the application of multidisciplinary design optimization methodologies enhances collaborative efficiency among these groups, allowing for a more cohesive approach to design challenges (Brevault et al., 2017).

The objective is to minimize the overall cost of the line by simultaneously addressing design considerations (e.g., station space, cost), operational factors (e.g., cycle time, precedence constraints, resource availability), and designer preferences (e.g., task complexity) (Nag, 2023). This leads to a definition of crucial conditions for a company to be competitive on the market: quality, reduced time and low costs for the development of new products (Rihar, Žužek, Kušar, 2020).

## 1.3. Car dampers production process

The first stage of damper production is forming tubes from a sheet of steel. The cut steel strips undergo a forming process using rotating rollers and are automatically welded after shaping.

The finished tubes are cut to the appropriate length depending on the type of damper. For further

consideration, the definition of the damper type was adopted as a production reference, i.e. a set of parameters defining the purpose of the damper, its dimensions, functional parameters and appropriate settings of the production machines on the line. The length of the tube cutting is precisely defined in the damper design and varies depending on whether it is a pressure or external tube. The external tube usually goes through additional processes related to ensuring the appropriate interface between the damper and the car's steering knuckle, e.g. the compression process of one of the ends, welding the pin or the steering knuckle clamp.

In the production of twin-tube dampers, valves controlling the internal oil flow are installed in the pressure tube, as well as additional elements in the form of rings or springs, depending on the valve design.

The rolling machine crimps the valve end, closing the bottom of the pressure tube. The outer tube is closed with a cover with a welded mounting eye, which is the so-called basic system. The assembled subassembly can be loaded with the open part upwards onto the final assembly line, where the pressure tube subassembly with the piston rod is fitted and inserted. It is also filled with oil. Finally, the damper is closed by assembling a steel piston, pressure valve and piston rod guide with a seal. The gas component in the form of nitrogen is introduced before closing the piece. Finally, various types of connectors, sleeves or protective collars made of steel or rubber are assembled.

In the production of mono-tube dampers, the tube is manufactured in a similar way to the twin-tube outer tube. After closing on one side and welding, the tube ends are sent to a washer and then to the assembly line. There, the geometry is checked, oil is filled, the floating piston and piston rod unit are assembled, functional tests are performed, gas is filled and the other side of the cylinder is closed.

## 2. Damper assembly and testing line

### 2.1. Project main objective

The project aimed to develop and showcase a hybrid technological line for the assembly and testing of automotive dampers with various process improvements. Funding for R&D work was obtained. The project's outcomes were implemented within the operations of ELPLC S.A., under Priority Axis I of the Smart Growth Operational Program 2014-2020 – Support for R&D activities by enterprises. The initiation of this project was also driven by extensive

experience in designing machines and production lines for automotive industry, using concurrent engineering practices and tools.

### 2.2. Target market

The implementation of the Project's results directly addresses the identified needs of the OEM and Tier 1 companies operating in the global market. These needs are primarily related to increasing the efficiency and flexibility of technological processes associated with the assembly and testing of the functionality and quality of car dampers. The target group highlighted the necessity of solutions that will allow them to increase production capacity, be cost-effective in terms of purchase and maintenance, and accelerate the fulfillment of orders. Moreover, the technological lines should offer various quality improvements, such as increased accuracy in measuring the damping force or gas filling process optimization, and enable the customization of functionalities to adapt to constantly evolving market trends.

### 2.3. Purpose of the line

The line presented in the study (Figures 2, 3, 4) assembles a ready-made twin-tube cylinder with a piston rod subassembly and a floating piston. The input components are: a mono pipe closed on one side with a welded tip, a ready-made piston rod assembly, a cap, oil, nitrogen, and labels. At the output of the line, the assembled damper is expected, ready for final assembly. Modularity was assumed in order to flexibly adjust the pallet flow and exchange stations, as well as easy conversion to various references.

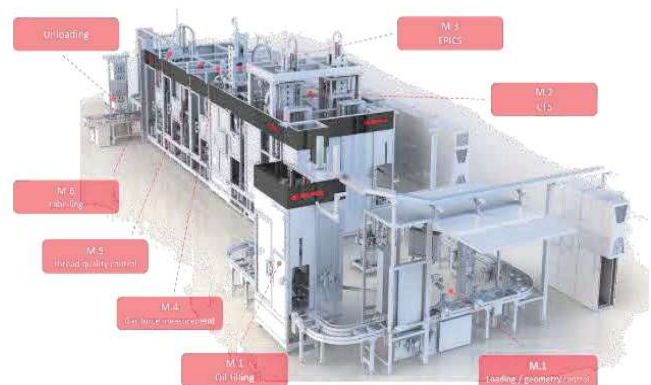


Fig. 2. 3D model with marked modules

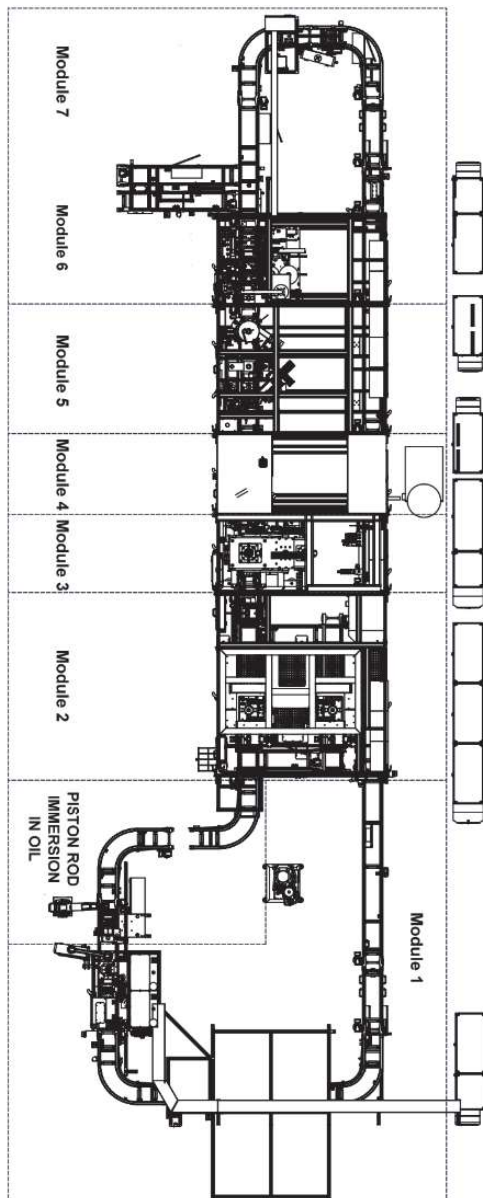


Fig. 3. Assembly line layout



Fig. 4. Assembly line panoramic photo

## 2.4. Main parameters for manufactured dampers

During development work, the widest possible range of line availability for typical product dimensions was taken into account (Table 2). At the same time, efforts were made to maintain the ease of re-tooling.

Table 2. Main parameters ranges

Parameter	Value, range
Tube diameter range	30 ÷ 60 mm
Tube height range	120 ÷ 600 mm
Product height range	120 ÷ 1000 mm
Maximum product weight	8 kg
Oil dosing volume	60 ÷ 600 ml
CTS <sup>1</sup> – test force	-6500 ÷ 6500 N
CTS – stroke range	0 ÷ 400 mm
CTS – test speed	0,5 ÷ 1000 mm/s
CTS – maximum acceleration	10 g
CTS – acceleration curves	sin, triangle, trapezoid
CTS – test frequency	16 Hz
Damper Closing Force (EPICS)	45 ÷ 150 kN
Gas pressure (EPICS)	2,5 MPa max.
Gas force control	20 ÷ 500 N
Cap diameter	40 ÷ 80 mm
Spring bed ring – diameter	30 ÷ 300 mm
Spring bed ring – position	25 ÷ 100 mm
Transport pallet size	320 x 320 mm

<sup>1</sup> CTS – functional characteristics tester.

## 2.5. Line modules

### 2.5.1. Module 1 – loading, geometry inspection, oil filling and assembly of the piston rod unit

The operator loads the finished pipe onto the transport pallet and confirms the loading. The pallet moves to a measuring gate that checks the pipe diameter and height, so that unsuitable or defective pipes can be eliminated at an early stage.

The inspection is carried out using a vision system with a fixed focal length lens. The system is mounted on an electric linear module with a maximum range of 600 mm (Fig. 5).

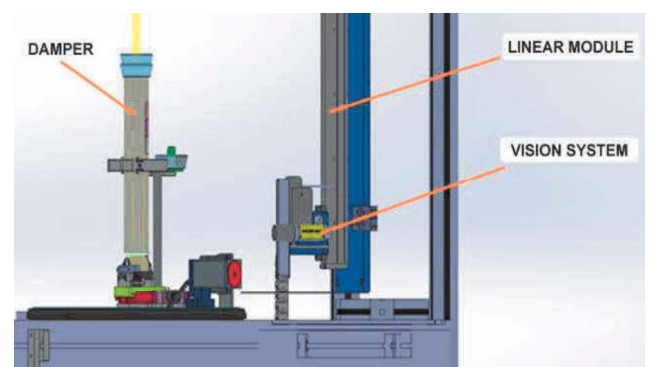


Fig. 5. Geometry control gate schematic

After positive geometry verification, the pallet moves automatically to the oil filling station. Oil is dosed into the damper chambers using a precise servomotor control algorithm and pneumatic solenoid valves. The maximum capacity of the filling cylinder is 780 ml. This allows dosing in the designed range of

60÷600 ml and avoiding operation over the full range of the actuator movement.

The piston rod insertion station in this module is prepared to be operated by a 6-axis universal robot that performs this monotonous and tedious operation.

### 2.5.2. Module 2 – functional characteristic tester

The actual measurement of the damping force is controlled using a force transducer with an appropriately increased range. The test force of 6.5 kN is confirmed by simulation with an additional margin. The force measurement is performed in a specific working position in range 0 to 400 mm.

Linear motors are characterized by maximum operating dynamics, allowing them to achieve high speeds quickly. The movement per unit of time is monitored using an external measurement system controlled by real-time systems.

The dynamics of the system related to its mechanical structure (Fig. 6), the path measurement resolution and the stability of readings allow for a wide range of speeds from 0.5 mm/s to 1500 mm/s. This range is also sufficient to perform functional tests of most dampers manufactured on the market.



Fig. 6. CTS testing tooling

### 2.5.3. Module 3 – closing and gas filling (EPICS)

Closing the damper consists in rounding the upper part of the tube while simultaneously gassing and maintaining the appropriate gas pressure in the damper.

The closing system is driven by a servo drive (Fig. 7). Then, a planetary screw coupled to the gas-rolling head is driven by a gear (Fig. 7). The system reaches the point where a specific force value occurs. The path is therefore dependent on the point where the set force occurs, and this depends on the type (production reference) of the damper and its dimensions,

and is therefore insensitive to the tolerance of the length of the tubes.

The aim of developing the station was to reduce cycle time, which was achieved by integrating two operations in one machine. In classic solutions, the gas filling with initial closing and final closing stations are separated. The result of the development of EPICS is over 50% shorter cycle time. Use of real-time system and single cycle chart makes data analysis simpler.

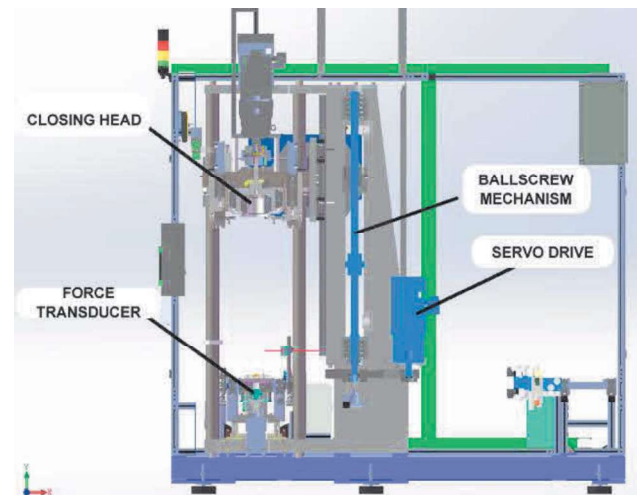


Fig. 7. EPICS station main elements

The force measurement is performed using a resistance strain gauge with a range of 250 kN. It allows for the measurement of forces in the assumed range from 45 kN to 150 kN. Oversizing the transducer allows for increasing the durability of the system thanks to a significant range reserve and resistance to significant exceedances of the assumed range.

At the EPICS station, nitrogen pressure in the damper is achieved up to 2,5 MPa. A dedicated pneumatic system and a head and cylinder sealing assembly have been designed for this purpose (Fig. 7). Nitrogen under pressure is supplied to the damper in the closing head.

### 2.5.4. Module 4 – gas force measurement

Gas force control in the typical range of 20-500N is a way to assess the correctness of the Module 3 (EPICS) operations. The measurement is carried out using a resistance strain gauge with a range of 1.25 kN and a dedicated rotation system (Fig. 8). The adopted range of force values is typical for the vast majority of dampers manufactured. Module 4 also includes a piston rod thread blow-out system. Contaminants on the thread could falsify the result of the visual thread inspection on the next module.

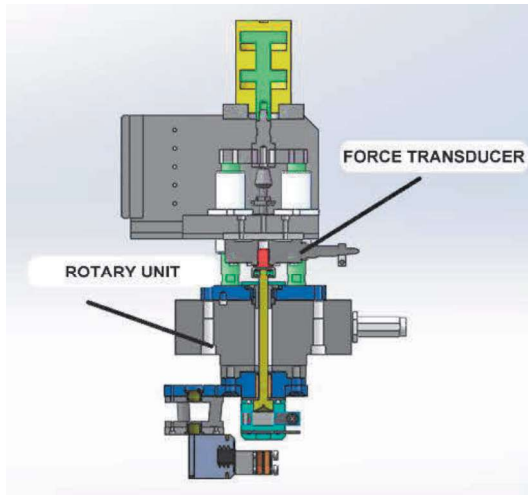


Fig. 8. Gas force test unit

### 2.5.5. Module 5 – Thread quality control and cap assembly

The cap diameter taken from the transport pallet depends on the shape and dimensions of the gripper jaws (Fig. 9; Fig. 10). Thanks to the retoolable jaws (yellow elements on Fig. 9 and Fig. 10), it is possible to ensure clamping of the overlay with a diameter in the range of 40-80 mm. For typical products on the line, a gripper with a stroke of 30 mm per jaw, a closing force of 260 N and an opening force of 300 N was selected. The gripping system was equipped with a special system for quick jaw retooling with positioning. Below is a simulation of the clamping possibilities of jaws designed for diameters of 60 mm (Fig. 9). Additionally, the station has thread quality control performed by an original vision system with hi-res cameras.

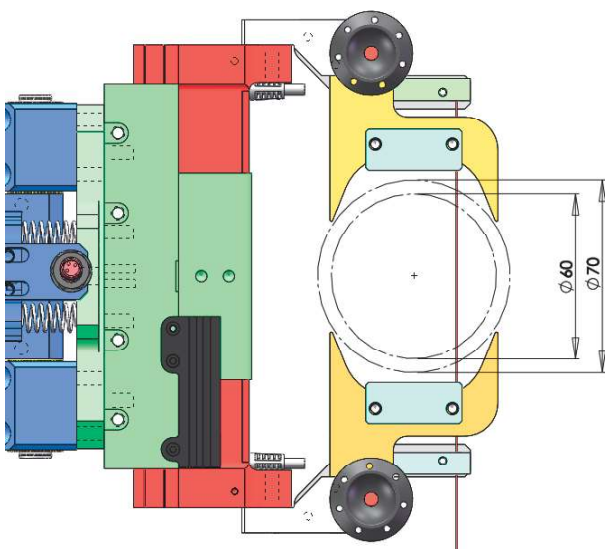


Fig. 9. Cap gripper jaws – open position

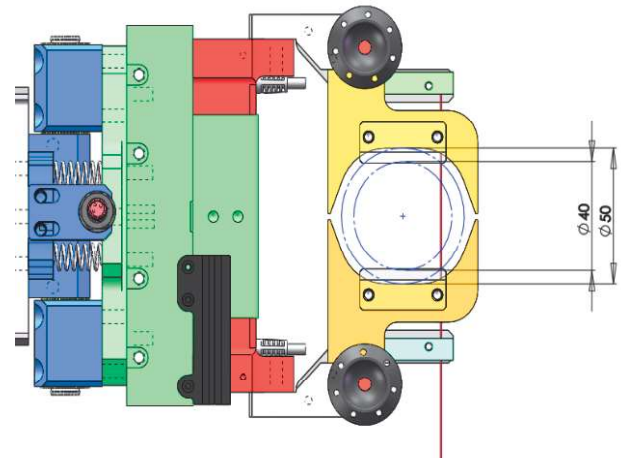


Fig. 10. Cap gripper jaws – open position

It is important to consider the clearance needed when the jaws approach the cap and the proper adhesion and holding of the cap after crimping. Another limitation is the distance between the cap collection point and its mounting point on the damper. In our case, it is 90 mm x 90 mm. This is a range optimally selected for the typical cap diameters.

### 2.5.6. Modules 6 and 7 – labelling, final control and unloading

The final stage of the production flow is labeling the damper, final inspection and unloading for further assembly. The presented line was based on a Bosch Rexroth BS 2/R series transport system with a metal accumulation chain. The load capacity of the transport drive is 1.5 kg/cm, which means that the weight of the 320x320 mm pallet with the component cannot exceed 48 kg. The recommended optimal range for this transport system is 20-25 kg, the project assumed 23 kg. The pallet itself with the socket and RFID carrier weighs approx. 15 kg, which gives us a possible maximum component weight up to 8 kg. This is supported by ergonomic considerations and typical values for manufactured dampers. Before unloading, the damper passes through the final inspection station. The following product parameters are checked using a vision system:

- Tube diameter: 30÷60 mm,
- Tube height: 120÷600 mm,
- Spring bed ring position: 25÷100 mm,
- Product height: 300÷1000 mm.

## 3. Summary

The planned milestones in the form of individual modules and the following innovative features of the line were achieved:

- a) modularity of the installation,

- b) high accuracy of measurement on testing stations,
- c) high automation of the technological line, robotization of piston rod immersion,
- d) cycle time reduction (gas filling and closing module),
- e) increased service life of modules / technological line.

The designed and built technological line meets required parameters covering a wide group of typical dampers manufactured in the world (see Table 2). After completing the design, assembly and programming work, the line was launched. A test run of components was carried out on each of the modules and their verification after the process and reference values were set. All modules have been validated in test production using real components. Finally only 2 operators are required for full service of the line – at the loading station (module 1) and unloading (module 7).

## Acknowledgments

Work on the POIR 01.01.01.01-00-1029/17-00 project "Development and demonstration of a modular technological line for assembly and testing of automotive dampers" was completed by ELPLC S.A. according to plan between July 1, 2018 and January 29, 2021. The project received funding under the Smart Growth Operational Program 2014-2020. As a result of this work, a detailed concept, design, and assembly line for dampers consisting of the modules described in this publication were created and tested.

All work was supervised by a team led Robert Tomasiewicz. The research team carried out conceptual work under the leadership of Piotr Brzyszczyk, with the support of Grzegorz Domagała. The team of programmers carried out work under the leadership of Sławomir Gleisner. Technologists – Anna Bąk and Wojciech Noga were responsible for preparing the documentation for production. The automation team carried out the work under the management of Tomasz Soboń. The mechatronics team carried out the work under the management of Paweł Tryba. As a result of the work of the R&D staff, full 2D and 3D documentation was prepared for future use.

## References

- Adham, A. A., Zainuddin, H. B., Siali, F. B., Azizan, N. A. (2013). *Assembly line balancing in manufacturing processes: using simulation model* (Advanced Materials Research, 748, pp. 1183–1187).
- Bortolini, M., Ferrari, E., Gamberi, M., Pilati, F., & Faccio, M. (2017). *Assembly system design in the industry 4.0 era: a general framework*. (IFAC-PapersOnLine, 50(1), 5700–5705).
- Brevault, L., Balesdent, M., & Defoort, S. (2017). *Preliminary study on launch vehicle design: applications of multi-disciplinary design optimization methodologies*. (Concurrent Engineering, 26(1), pp. 93–103).
- Cohen, Y. (2013). *Assembly line segmentation: determining the number of stations per section*. (Journal of Manufacturing Technology Management, 24(3), pp. 397–412).
- Czop P., Sawik D. (2011). *A high-frequency first-principle model of a shock absorber and servohydraulic tester* (Mechanical Systems and Signal Processing 25(6), August 2011; pp. 1937–1955).
- Duym S., Steins R., Reybrouck K. (1997) *Evaluation of shock absorber models*, *Vehicle System Dynamics* (International Journal of Vehicle Mechanics and Mobility 27(2)/1997; pp. 109–127).
- Farjoud A., Ahmadian M., Craft M., Burke W. (2012). *Nonlinear modeling and experimental characterization of hydraulic dampers: effects of shim stack and orifice parameters on damper performance*, (Nonlinear Dynamics, Vol. 67, Issue 2, January 2012, pp. 1437–1456).
- Ferdek U., Luczko J. (2012). *Modeling and analysis of a twin-tube hydraulic shock absorber*, (Czasopismo Techniczne, 2-M/2012, pp. 627–638).
- Gao, S., Jin, R., & Lu, W. (2019). *Design for manufacture and assembly in construction: a review*. (Building Research & Information, 48(5), pp. 538–550).
- Gardulski J., (2009). *Metody badań amortyzatorów samochodów osobowych*, (DIAGNOSTYKA' 3(51)/2009).
- Lang H. H., (1977). *A study of the characteristics of automotive hydraulic dampers at high stroking frequencies*, The University of Michigan, 1977.
- Nag, M. (2023). *Significance of concurrent engineering methods used in automotive industries*. (International Journal of Scientific Research in Engineering and Management, 07(03)).
- Nourmohammadi, A. and Eskandari, H. (2017). *Assembly line design considering line balancing and part feeding*. (Assembly Automation, 37(1), pp. 135–143).
- Rihar, L., Žužek, T., & Kušar, J. (2020). *How to successfully introduce concurrent engineering into new product development?* (Concurrent Engineering, 29(2), pp. 87–101).
- Shelton, Ch., (2017). *Then, Now, and Forever* (Hot Rod, March 2017, pp. 16–29).
- Sikora M., (2017). *Pomiary drgań i ciśnienia w amortyzatorze hydraulicznym w zawieszeniu samochodowym*, (Technical Transactions 4/2017, pp. 210–217)
- Triki, H., Hachicha, W., & Masmoudi, F. (2017). *Manufacturing system design based on axiomatic design: case of assembly line*. (Journal of Industrial Engineering and Management, 10(1), p. 111).
- Yamada, T., Miyauchi, T., & Sugi, M. (2022). *2-stage design for a hybrid assembly line with humans and robots considering automation difficulty level: case study of the electrical equipment assembly line*. (International Journal of Smart Computing and Artificial Intelligence, 6(1)).
- Persistence Market Research (2023). *Automotive Shock Absorbers Market Outlook (2023 to 2033)*. <https://www.persistencemarketresearch.com/market-research/shock-absorbers-market.asp>.